DISSERTATION

EMERGENT TOPOLOGICAL PHENOMENA IN LOW-D SYSTEMS INDUCED BY GAUGE POTENTIALS

Submitted by

Aidan Winblad

Department of Physics

In partial fulfillment of the requirements

For the Degree of Doctor of Philosophy

Colorado State University

Fort Collins, Colorado

Summer 2024

Doctoral Committee:

Advisor: Hua Chen

Richard Eykholt
Martin Gelfand
Olivier Pinaud

ABSTRACT

EMERGENT TOPOLOGICAL PHENOMENA IN LOW-D SYSTEMS INDUCED BY GAUGE POTENTIALS

Abstract goes here

ACKNOWLEDGEMENTS

I would like to thank the CSU Graduate Student Council and the CSU Graduate School for initiating, commissioning and supporting this project. I would also like to thank Nicole Ramo for her support and ensuring that we followed through with this project to completion. I would like to thank Leif Anderson, who created and supported the previous LaTeX template for a number of years. Although I have never met Leif, his work was invaluable in the creation of this package and has helped many students get their thesis approved by the CSU graduate school. Finally, I would like to thank everyone who helps to contribute to this package. Your work will help many CSU graduate students to create professional, beautiful and compelling theses and dissertations using LaTex. Last but not least, thank you to the creators and maintaners of LaTeX for creating a fantastic typesetting tool.

DEDICATION

I would like to dedicate this dissertation to my dog Zeta.

TABLE OF CONTENTS

LIST OF TABLES

Chapter 1

Introduction

EM gauge potential appears in electronic Hamiltonian in CM

1. Review Maxwell theory -> gauge potential
2. Minimal coupling $-i\hbar\nabla \rightarrow -i\hbar\nabla + q\mathbf{A}$ or $-i\partial_\mu \rightarrow -i\partial_\mu + qA_\mu$
3. TB Hamiltonian and Peierls phase

Topological phenomena in CM considered in thesis

1.1 Introduction

Hello, here is the introduction.

1.2 Maxwell's equations

In this dissertation we use gauge potentials as the key ingredient for inducing topological phase transitions in condensed matter systems, such as superconductors and insulators. A quick review of gauge potentials and gauge invariance will help set the stage for the manipulations we do in later chapters. Let us start with Maxwell theory, given by the following equations,

$$\nabla \cdot \mathbf{E} = \frac{1}{\epsilon_0}\rho \tag{1.1}$$

$$\nabla \cdot \mathbf{B} = 0 \tag{1.2}$$

$$\nabla \times \mathbf{E} = -\partial_t \mathbf{B} \tag{1.3}$$

$$\nabla \times \mathbf{B} = \mu_0 \mathbf{J} + \mu_0 \epsilon_0 \partial_t \mathbf{E}. \tag{1.4}$$

We want to write Maxwell's equations in terms of potentials, V and $\mathbf{A}$. The magnetic field in terms of a vector potential is $\mathbf{B} = \nabla \times \mathbf{A}$. This lets us rewrite Eq. (1.3) as

$$\nabla \times (\mathbf{E} + \partial_t \mathbf{A}) = 0 \tag{1.5}$$

$$\mathbf{E} = -\nabla V - \partial_t \mathbf{A}. \tag{1.6}$$

As a check, if $\mathbf{A} = \text{const}$, then $\mathbf{E} = -\nabla V$ as expected. With a new definition of the electric field we look at Eq. (1.1) to arrive at

$$\nabla \cdot \mathbf{E} = \nabla \cdot (-\nabla V - \partial_t \mathbf{A}) \tag{1.7}$$

$$= -\nabla^2 V - \partial_t \nabla \cdot \mathbf{A} = \frac{1}{\epsilon_0}\rho. \tag{1.8}$$

Now we manipulate Eq. (1.4) to give

$$\nabla \times \mathbf{B} = \nabla \times (\nabla \times \mathbf{A}) \tag{1.9}$$

$$= \nabla(\nabla \cdot \mathbf{A}) - \nabla^2 \mathbf{A} \tag{1.10}$$

$$= \mu_0 \mathbf{J} + \mu_0 \epsilon_0 \left(-\nabla \partial_t V - \partial_t^2 \mathbf{A}\right). \tag{1.11}$$

Which we rearrange to

$$-\mu_0 \mathbf{J} = \nabla^2 \mathbf{A} - \mu_0 \epsilon_0 \partial_t^2 \mathbf{A} - \nabla\left(\nabla \cdot \mathbf{A} + \mu_0 \epsilon_0 \partial_t V\right). \tag{1.12}$$

We have thus shown Maxwell's equations in terms of potentials.

1.3 Gauge transformations

We now move on to gauge transformations. Suppose $\mathbf{A}' = \mathbf{A} + \boldsymbol{\alpha}$ and $V' = V + \beta$. Both vector potentials give the same magnetic field,

$$\mathbf{B} = \nabla \times \mathbf{A} = \nabla \times \mathbf{A}' = \nabla \times (\mathbf{A} + \boldsymbol{\alpha}) \tag{1.13}$$

$$\nabla \times \boldsymbol{\alpha} = 0 \tag{1.14}$$

$$\boldsymbol{\alpha} = \nabla\lambda. \tag{1.15}$$

The two potentials should also give the same electric field,

$$\mathbf{E} = -\nabla V - \partial_t \mathbf{A} \tag{1.16}$$

$$= -\nabla V' - \partial_t \mathbf{A}'$$

$$= -\nabla V - \nabla\beta - \partial_t \mathbf{A} - \partial_t \boldsymbol{\alpha}$$

$$\text{then} \quad 0 = \nabla\beta + \partial_t \boldsymbol{\alpha} \tag{1.17}$$

$$= \nabla\beta + \partial_t \nabla\lambda$$

$$= \nabla(\beta + \partial_t \lambda)$$

$$\beta = -\partial_t \lambda + k(t)$$

$$\beta = -\partial_t \tilde{\lambda}$$

$$\mathbf{A}' = \mathbf{A} + \nabla\lambda \tag{1.18}$$

$$V' = V - \partial_t \tilde{\lambda} \tag{1.19}$$

From the above set of expressions we arrive at the general gauge transformations of potentials. We make note that a change in V and $\mathbf{A}$ does not change the electric and magnetic fields, gauge invariant, and are used to adjust the divergence of $\mathbf{A}$. This allows to solve the scalar and vector potentials readily depending on the gauge. We will next go over two most common gauge choices, Coulomb and Lorenz.

1.3.1 Coulomb gauge

The Coulomb gauge is used in the case of magnetostatics. We assert the following for a Coulomb gauge, $\nabla \cdot \mathbf{A} = 0$, which makes $\nabla^2 V = -\frac{1}{\epsilon_0}\rho$. Recall Eq. (1.12), it simplifies to

$$\begin{aligned} \left(\nabla^2 - \mu_0\epsilon_0\partial_t^2\right)\mathbf{A} &= -\mu_0\mathbf{J} + \mu_0\epsilon_0\nabla\partial_t V \\ \Box^2\mathbf{A} &= -\mu_0\mathbf{J} + \mu_0\epsilon_0\nabla\partial_t V \end{aligned} \tag{1.20}$$

where we have used $\Box$ as the d'Alembertian.

1.3.2 Lorenz gauge

Here we instead assert $\nabla \cdot \mathbf{A} = -\mu_0\epsilon_0\partial_t V$, which makes $\Box^2\mathbf{A} = -\mu_0\epsilon_0\mathbf{J}$. Recall Eq. (1.8), it simplifies to

$$\begin{aligned} \nabla^2 V + \partial_t(\nabla\cdot\mathbf{A}) &= \nabla^2 V - \mu_0\epsilon_0\partial_t^2 V \\ \Box^2 V &= -\frac{1}{\epsilon_0}\rho \end{aligned} \tag{1.21}$$

We can now clearly see how the two gauges affect our potentials. The Lorenz gauge has the advantage of treating both scalar and vector potential with the same d'Alembertian operator, thus readily able to solve both scalar and vector potentials. The Coulomb gauge allows for an

easily calculable scalar potential, however, it is murkier solve for the vector potential. REFERENCE GRIFFITHS introduction to electrodynamics 4th Edition

1.4 Minimal coupling and Canonical momentum

Minimal coupling comes from the following substitution

$$-i\hbar\nabla \rightarrow -ih\nabla - q\mathbf{A}, \tag{1.22}$$

which can be derived from the canonical momentum operator when a charged particle is present in a vector potential field. In this case minimal coupling means the field is coupling the orbital and potential only, ignoring higher order multipole moments. This also allows the system to have a local gauge invariance under U(1) transformations, i.e. $\mathbf{A} \rightarrow \mathbf{A} + \nabla\lambda$. REFERENCE Alexander Atlan Condensed Matter Field Thoery.

We will next derive the canonical momentum operator and demonstrate its gauge invariance. Simply start with the Lagrangian for charged particle in a scalar and vector potential field,

$$\begin{aligned} \mathscr{L} &= T - U \\ \mathscr{L} &= \frac{1}{2}m\dot{r}^2 - qV + q\dot{\mathbf{r}}\cdot\mathbf{A}(\mathbf{r},t), \end{aligned} \tag{1.23}$$

where $T = \frac{1}{2}m\dot{r}^2$ and $U = qV - q\dot{\mathbf{r}}\cdot\mathbf{A}(\mathbf{r},t)$. One recalls from classical mechanics that

$$\mathbf{p} = \frac{\partial \mathscr{L}}{\partial \dot{\mathbf{r}}}$$

$$\mathbf{p} = m\dot{\mathbf{r}} + q\left(\partial_{\dot{x}} + \partial_{\dot{y}} + \partial_{\dot{z}}\right)\left(\dot{x}A_x + \dot{y}A_y + \dot{z}A_z\right)$$

$$\mathbf{p} = m\mathbf{v} + q\mathbf{A}$$

$$\mathbf{p}_{can} = \mathbf{p}_{kin} + q\mathbf{A} \tag{1.24}$$

Now that we know the canonical momentum and defined the Lagrangian we can determine the Hamiltonian

$$\begin{aligned}
\mathscr{H} &= \mathbf{p}\cdot\dot{\mathbf{r}} - \mathscr{L} \\
&= (m\dot{\mathbf{r}} + q\mathbf{A})\cdot\dot{\mathbf{r}} - \frac{1}{2}m\dot{r}^2 + qV - q\dot{\mathbf{r}}\cdot\mathbf{A} \\
&= \frac{1}{2}m\dot{r}^2 + qV \\
&= \frac{1}{2m}p_{kin}^2 + qV \\
\mathscr{H} &= \frac{1}{2m}(\mathbf{p}_{can} - q\mathbf{A})^2 + qV,
\end{aligned} \tag{1.25}$$

where in the last step we used Eq. (1.24) to replace the kinetic momentum. Thus we have shown that in the presence of a vector potential field we have the minimal coupling expression $i\hbar\nabla - a\mathbf{A}$.

Next, for simplicity, we show the previous Hamiltonian without a scalar potential is gauge invariant (it can be shown with the scalar potential but it is irrelevant to our research). Suppose $\mathscr{H}|\psi\rangle = \epsilon|\psi\rangle$ and that

$$\mathscr{H} = \frac{1}{2m}(\mathbf{p} - q\mathbf{A})^2. \tag{1.26}$$

Let $\mathbf{A}' = \mathbf{A} + \nabla\lambda$, where λ is a scalar. Then,

$$\mathscr{H}|\psi\rangle = \frac{1}{2m}(\mathbf{p} - q\mathbf{A}' + q\nabla\lambda)^2|\psi\rangle = \epsilon|\psi\rangle, \tag{1.27}$$

and also allow

$$\begin{aligned}\mathscr{H}'|\psi'\rangle &= \frac{1}{2m}(\mathbf{p} - q\mathbf{A}')^2|\psi'\rangle, \\ \mathscr{H}'|\psi'\rangle &= \frac{1}{2m}(\mathbf{p} - q\mathbf{A} - q\nabla\lambda)^2|\psi'\rangle = \epsilon|\psi'\rangle.\end{aligned} \tag{1.28}$$

Let $|\psi'\rangle = U|\psi\rangle$, where U is a unitary operator such that $U^\dagger U = \mathbf{1}$. Position and Momentum expectations should be the same under both gauge choices. Starting with position we derive one useful commutation relation

$$\begin{aligned}\langle\psi'|\mathbf{r}|\psi'\rangle &= \langle\psi|U^\dagger\mathbf{r}U|\psi\rangle = \langle\psi|\mathbf{r}|\psi\rangle \\ U^\dagger\mathbf{r}U &= \mathbf{r} \\ \mathbf{r}U &= U\mathbf{r} \\ [\mathbf{r}, U] &= 0.\end{aligned} \tag{1.29}$$

We can then extrapulate to $[\mathbf{A}, U] = 0$. With momentum we can derive another useful commutation relation

$$\langle\psi'|\mathbf{p}-q\mathbf{A}'|\psi'\rangle = \langle\psi|U^\dagger(\mathbf{p}-q\mathbf{A}')U|\psi\rangle = \langle\psi|\mathbf{p}-q\mathbf{A}|\psi\rangle$$

$$U^\dagger\mathbf{p}U - U^\dagger q\mathbf{A}'U = \mathbf{p}-q\mathbf{A}$$

$$\mathbf{p}U - q\mathbf{A}U - q\nabla\lambda U = U\mathbf{p} - Uq\mathbf{A}$$

$$[\mathbf{p},U] = -i\hbar\partial_{\mathbf{r}}U = q\nabla\lambda U. \tag{1.30}$$

This leads us to find $U = \exp\left[iq\lambda/\hbar\right]$ We can now look at the Hamiltonian and see how each gauge relates to each other

$$\begin{aligned}\mathscr{H}'|\psi'\rangle &= (\mathbf{p}-q\mathbf{A}-q\nabla\lambda)^2|\psi'\rangle \\ &= (\mathbf{p}-q\mathbf{A}-q\nabla\lambda)\cdot(\mathbf{p}U-q\mathbf{A}U-q\nabla\lambda U)|\psi\rangle \\ &= (\mathbf{p}-q\mathbf{A}-q\nabla\lambda)\cdot U(\mathbf{p}-q\mathbf{A})|\psi\rangle \\ &= U(\mathbf{p}-q\mathbf{A})^2|\psi\rangle \\ &= U\epsilon|\psi\rangle. \end{aligned} \tag{1.31}$$

We see the local phase of the wavefunction is changed but it still represents the same energy shown by

$$\langle\psi'|\mathscr{H}'|\psi'\rangle = \langle\psi|U^\dagger U\epsilon|\psi\rangle = \epsilon$$

$$\langle\psi|\mathscr{H}|\psi\rangle = \langle\psi|\epsilon|\psi\rangle = \epsilon, \tag{1.32}$$

and in other words $U^\dagger\mathscr{H}'U = \mathscr{H}$. REFERENCE Kittel Introduction to solid state physics.

1.5 Peierls phase in tight-binding models

We next show how to incorporate a vector potential field into a tight-binding Hamiltonian. There are a few ways to derive a Peierls phase and we will use the differential geometry approach. Before we showed minimal coupling and now we would like to express it in terms of a covariant derivative

$$D_\mu = \partial_\mu - iA_\mu. \tag{1.33}$$

Let us now envision how a wavefunction will evolve in the presence of a vector potential field. Using the covariant derivative with the parallel transport along curves we can obtain an expression for the phase accumulation on the wave function. The covariant derivative should vanish if it is parallel transported along the curve $\mathscr{C}$ defined by points x and $x' = x + vt$. The expression is as follows

$$\begin{aligned}
\nabla_v s = 0 \rightarrow & tv^\mu D_\mu s_{x(t)} = 0 \\
& = t\dot{x}^\mu(t)(\partial_\mu - iA_u)s_{x(t)} \\
& = t\frac{\partial x^\mu}{\partial t}\frac{\partial}{\partial x_\mu}s_{x(t)} - it\dot{x}^\mu(t)A_{x(t),\mu}s_{x(t)} \\
\rightarrow & \dot{s}_{x(t)} - i\dot{x}^\mu(t)A_{x(t),\mu}s_{x(t)} = 0 \\
\rightarrow & s_{x(t)} = s_{x(0)}\exp\left[i\int_0^t \dot{x}^\mu A_{x(t'),\mu}dt'\right] \\
& s_{x(t)} = s_{x(0)}\exp\left[i\int_{\mathscr{C}} dx^\mu A_{x(t'),\mu}\right]
\end{aligned} \tag{1.34}$$

and in general we can rewrite to the following expression $\psi(t) = \psi(0)\exp\left[\frac{iq}{\hbar}\int_{\mathscr{C}}\mathbf{A}(\mathbf{r})\cdot d\mathbf{l}\right]$.

Given the following tight-binding Hamiltonian

$$\mathscr{H}_t = -t \sum_{\langle j,l \rangle} c_j^\dagger c_l + h.c., \tag{1.35}$$

we can apply a vector potential to a system making the following Peierls phase transform, a unitary transform, to its creation/annihilation operators

$$\begin{aligned} c_j &\rightarrow c_j \exp\left[\frac{iq}{\hbar}\int^{\mathbf{r}_j} \mathbf{A}\cdot d\mathbf{l}\right] \\ c_j^\dagger c_l &\rightarrow c_j^\dagger c_l \exp\left[\frac{iq}{\hbar}\int_{\mathbf{r}_j}^{\mathbf{r}_l} \mathbf{A}\cdot d\mathbf{l}\right]. \end{aligned} \tag{1.36}$$

The Hamiltonian in the new basis takes the following form

$$\mathscr{H}_t = \sum_{\langle j,l \rangle} -t_{j,l} c_j^\dagger c_l + h.c., \tag{1.37}$$

where $t_{j,l} = t \exp\left[\frac{iq}{\hbar}\int_{\mathbf{r}_j}^{\mathbf{r}_l} \mathbf{A}\cdot d\mathbf{l}\right]$.

1.6 Majorana fermions and Topological superconductors

In brief, Majorana Ettore hypothesised the existence of Majorana fermions, by finding a unique (real) wavefunction solution to Dirac's equation, who found a general (complex) wavefunction solution. The Standard Model predicts neutrinos to be Majorana fermions yet that has yet to be measured. One can achieve a Majorana fermion as a linear combination of two fermions, also known as a Bogoliubov quasiparticle, inside a non-trivial topological p-wave superconductor. We have yet to physically realize a p-wave superconductor experimentally, however, we can use heterostructures in proximity to an s-wave superconductor to achieve an effective p-wave superconduting interface, which is explained and referenced in later chapters. Majorana fermions are dictated by non-Abelian exchange statistics, which allows for building a universal quantum computer, hence why they are highly sought after. Another boon of using

a non-trivial topological superconductor is the ability to protect Majorana fermions from local perturbations.

One of our goals in this disseration is present a new type of topological quantum logic gate that utilizes triangular geometry and rotation of a vector potential field to host and braid Majorana fermions.

Let us go ahead and show how Kitaev derived Majorana zero modes, Majorana fermions, on a 1D spinless p-wave superconductor. Start with a 1d spinless p-wave superconductor tight-binding Hamiltonian

$$\mathscr{H} = \sum_{j}^{N-1} (-t c_j^\dagger c_{j+1} + \Delta c_j c_{j+1} + h.c.) - \sum_{j}^{N} \mu c_j^\dagger c_j, \tag{1.38}$$

where t is hopping amplitude, superconducting order parameter $\Delta = |\Delta|$ for simplicity, μ is chemical potential, and $c^\dagger(c)$ is the creation (annihilation) operator for a complex fermion. We next use a basis tranformation to convert to the Majorana fermion basis, where $c_j^\dagger = \frac{1}{2}(a_j - i b_j)$, $\left\{a_j^\dagger, a_{j'}\right\} = \{a_j, a_{j'}\} = 2\delta_{j,j'}$ since they are Majorana fermions, and $\left\{a_j, b_j'\right\} = 0$. After some algebra we arrive at

$$\mathscr{H} = \frac{i}{2} \sum_{j} \left(-\mu a_j b_j + (t+\Delta) b_j a_{j+1} + (-t+\Delta) a_j b_{j+1}\right). \tag{1.39}$$

In the trivial phase, no Majorana fermions, $\mu \neq 0$ and $t = \Delta = 0$,

$$\mathscr{H} = -\mu \frac{1}{2} \sum_{j} a_j b_j. \tag{1.40}$$

The non-trivial phase, with Majorana fermions present, $\mu = 0$, and $t = \Delta > 0$,

$$\mathscr{H} = i t \sum_{j} b_j a_{j+1}. \tag{1.41}$$

Notice the terms a_0 and b_N are missing in the non-trivial Hamiltonian, we can say there is a non-localized zero energy mode present in the system defined by $f = \frac{1}{2}(a_0 + i b_N)$, hence the

name Majorana zero modes. Now, slightly outside the Kitaev limit for non-trivial topology, we can limit $|\mu| < 2t$ and $t = |Delta| > 0$ and still achieve non-trivial topology with Majorana zero modes at the interface of trivial and non-trivial topology. To understand why this is still true we can determine the topological invariant for the system, also known as the Majorana number, a type of Winding number for 1D superconducting systems. Calculating the Majorana number is straight forward enough, its proof on the other hand is not, this can be found in the appendix REFERENCE appendix here. Write the Hamiltonian in the Majorana basis, $A = -iU\mathscr{H}U^{\dagger}$, then take the sign of the Pfaffian,

$$\mathscr{M} = \text{sgn}[\text{Pf}(A)]. \tag{1.42}$$

This calculation can be reduced down if we can write the Hamiltonian in momentum space. Doing so lets us consider the $k = 0$ and $k = \pi$ points only in the brillouin zone, due to symmetry.

$$\mathscr{M} = \begin{cases} \text{sgn}[\text{Pf}(A_{k=0})\text{Pf}(A_{k=\pi})], & \text{if L is even,} \\ \text{sgn}[\text{Pf}(A_{k=0})], & \text{if L is odd,} \end{cases} \tag{1.43}$$

where L is the number of lattice sites from our lattice Hamiltonian. We find that under the Kitaev limit, if $|\mu| < 2t$, then $\mathscr{M} = -1$, and if $|\mu| > 2t$, then $\mathscr{M} = 1$. When a section of the material is in a non-trivial topology and either the other material is trivial or vacuum (also trivial), Majorana zero modes will be localized at the differing topological interfaces, this is also known as bulk-edge correspondence and will be used later in our topological quantum logic gate. As a last note, when $|\mu| = 2t$ this is a critical point and where the gap opens and closes, it is not an ideal region of parameter space for our needs.

Add in some schematics of Kitaev chain in the various cases described

1. Braiding (Application in TQC) not sure how much to talk about here, and slightly mentioned earlier with topological superconductors.

1.7 Landau levels in condensed matter

We are also interested in producing Landau levels in 2DEG and Dirac models using non-uniform circularly polarized laser light. To understand how Landau levels appear we need to solve the Hamiltonian associated with a 2DEG in the presence of a Magnetic field. We can start with the square lattice tight-binding Hamiltonian for a 2DEG

$$\mathscr{H} = -\sum_{\langle j,l\rangle} t c_j^\dagger c_l + h.c., \tag{1.44}$$

and in momentum space

$$\mathscr{H} = -\sum_{\mathbf{p}} 2t\left(\cos(p_x a) + \cos(p_y a)\right) c_{\mathbf{p}}^\dagger c_{\mathbf{p}}. \tag{1.45}$$

Then in the limit of small momenta k we arrive at

$$\begin{aligned}\mathscr{H} &= -\sum_{\mathbf{p}} 2t\left(2 - \frac{p_x^2 a^2}{2} - \frac{p_y^2 a^2}{2}\right) c_{\mathbf{p}}^\dagger c_{\mathbf{p}},\\ \mathscr{H}(\mathbf{p}) &= \left(\frac{p_x^2 + p_y^2}{2m}\right),\end{aligned} \tag{1.46}$$

we have thus arrived at Schrodingers equation for a 2DEG in the limit of small momenta. Let us assume a 2DEG in the x-y plane and has a magnetic field that points in the positive $\mathbf{z}$ direction, $\mathbf{B} = B\mathbf{z}$ or $\mathbf{A} = Bx\mathbf{y}$. The Hamiltonian in momentum space then becomes

$$\mathscr{H} = \frac{1}{2m}\left(\hat{p}_x^2 + (\hat{p}_y - qB\hat{x})^2\right) \tag{1.47}$$

Recall $[\hat{r}_\alpha, \hat{p}_\beta] = i\hbar\delta_{\alpha,\beta}$, that means our magnetic term commutes with $\hat{p}_y$, so let us assume that $\Psi(x,y) = e^{ik_y y}\psi(x)$. Acting the Hamiltonian on the ansatz wavefunction yields

$$\mathscr{H}\Psi = \frac{1}{2m}\left(\hat{p}_x^2 + (qB\hat{x} - \hbar k_y)^2\right) e^{ik_y y}\psi(x)$$

$$\mathscr{H} = \frac{1}{2m}\left(\hat{p}_x^2 + q^2B^2\hat{x}^2\right)$$

$$= \frac{\hat{p}_x^2}{2m} + \frac{1}{2}m\omega^2\hat{x}^2, \tag{1.48}$$

where we let $x - \frac{\hbar k_y}{mqB} \to x$, since it is just a shift in x coordinates. Notice that we arrive at the expression for a quantum harmonic oscillator. A derivation for the energy solutions can be found in A.5. With the energy solutions

$$E_n = \hbar\omega\left(n + \frac{1}{2}\right) = \frac{\hbar qB}{m}\left(n + \frac{1}{2}\right). \tag{1.49}$$

An alteration to the lattice model can have slightly different results. Using a honeycomb lattice, provided by graphene, gives the following Hamiltonian

$$\mathscr{H} = -t\sum_{\substack{j,l \\ \alpha\beta}} c_{j\alpha}^\dagger c_{l\beta} + h.c., \tag{1.50}$$

with lattice vectors $\mathbf{a}_1 = \sqrt{3}a\mathbf{x}$ and $\mathbf{a}_2 = \frac{\sqrt{3}}{2}a\mathbf{x} + \frac{3}{2}a\mathbf{y}$. In momentum space

$$\mathscr{H} = -t\sum_{\mathbf{p}} \begin{bmatrix} 0 & 1 + e^{i\mathbf{p}\cdot\mathbf{a}_1} + e^{i\mathbf{p}\cdot\mathbf{a}_2} \\ 1 + e^{-i\mathbf{p}\cdot\mathbf{a}_1} + e^{-i\mathbf{p}\cdot\mathbf{a}_2} & 0 \end{bmatrix},$$

$$\mathscr{H}(\mathbf{p}) = \begin{bmatrix} 0 & t(\mathbf{p}) \\ t^*(\mathbf{p}) & 0 \end{bmatrix},$$

where the hopping can be rewritten as

$$t(\mathbf{p}) = -te^{i\sqrt{3}p_x a/2}\left(2\cos\left(\frac{\sqrt{3}p_x a}{2}\right) + e^{i3p_y a/2}\right) \tag{1.51}$$

which gives the following energy spectrum

$$E(\mathbf{p}) = \pm t\sqrt{3 + 2\cos\left(\sqrt{3}p_x a\right) + 4\cos\left(\frac{\sqrt{3}p_x a}{2}\right)\cos\left(\frac{3p_y a}{2}\right)}. \tag{1.52}$$

There are several high symmetry points on the corners of the Brillouin zone, one such point is $\mathbf{K} = \frac{4\pi}{3\sqrt{3}a}\mathbf{x}$. Going back to the Hamiltonian and expanding about $\mathbf{K}$ with small $\mathbf{q}$, $\mathbf{q} = \mathbf{p} + \mathbf{K}$, gives the following hopping amplitude

$$\begin{aligned}
t(\mathbf{q}) &= -te^{i\sqrt{3}q_x a/2}e^{i\sqrt{3}Ka/2}\left(2\cos\left(\frac{\sqrt{3}q_x a}{2} + \frac{\sqrt{3}Ka}{2}\right) + e^{i3p_y a/2}\right) \\
t(\mathbf{q}) &= -te^{i\sqrt{3}q_x a/2}e^{i2\pi/3}\left(2\cos\left(\frac{\sqrt{3}q_x a}{2} + \frac{2\pi}{3}\right) + e^{i3p_y a/2}\right) \\
t(\mathbf{q}) &= -te^{i\sqrt{3}q_x a/2}e^{i2\pi/3}\left(-\cos\left(\frac{\sqrt{3}q_x a}{2}\right) - \sqrt{3}\sin\left(\frac{\sqrt{3}q_x a}{3}\right) + e^{i3p_y a/2}\right) \\
t(\mathbf{q}) &\approx te^{i2\pi/3}\left(\frac{3q_x a}{2} - \frac{i3q_y a}{2}\right) \\
t(\mathbf{q}) &= v_f e^{i2\pi/3}\left(q_x - iq_y\right), \\
t^*(\mathbf{q}) &= v_f e^{-i2\pi/3}\left(q_x + iq_y\right),
\end{aligned}$$

where we keep the leading order in $\mathbf{q}$ and $v_f = \frac{3ta}{2}$. Using a gauge transformation and redefining $\mathbf{q} \to \mathbf{p}$ we arrive at the Dirac equation

$$\mathscr{H}(\mathbf{p}) = v_f \boldsymbol{\sigma}\cdot\mathbf{p}. \tag{1.53}$$

With graphene spanning the x-y plane in the presence of a magnetic field $\mathbf{B} = B\mathbf{z}$, $\mathbf{A} = Bx\mathbf{y}$, the Dirac equation becomes

$$\mathscr{H}(\mathbf{p}) = v_f \boldsymbol{\sigma}\cdot\left(\mathbf{p} - \mathbf{qA}\right). \tag{1.54}$$

A derivation for the energy solution can be found in A.6. The quantized energy solutions for a 2D Dirac equation in the presence of perpendicular magnetic field is

$$E_n = v_f \sqrt{2\hbar q B n} \tag{1.55}$$

Landau Level and Hofstadter butterfly

i solve for LL in 2DEG — why it's topological, chern number, TKNN quantum Hall

ii square lattice — hofstadter butterfly (on other lattices, honeycomb)

Chapter 2

Superconducting Triangular Islands as a Platform for Manipulating Majorana Zero Modes

2.1 Introduction

For more than twenty years, Majorana zero modes (MZM) in condensed matter systems have been highly sought after due to their potential for serving as building blocks of topological quantum computation, thanks to their inherent robustness against decoherence and non-Abelian exchange statistics [1–5]. MZM were originally proposed to be found in half-quantum vortices of two-dimensional (2D) topological p-wave superconductors and at the ends of 1D spinless p-wave superconductors [6, 7]. Whether a pristine p-wave superconductor [8] has been found is still under debate. However, innovative heterostructures proximate to ordinary s-wave superconductors have been proposed to behave as effective topological superconductors in both 1D and 2D. These include, for example, semiconductor nanowires subject to magnetic fields [9–11], ferromagnetic atomic spin chains [12–17], 3D topological insulators [18–21], quantum anomalous Hall insulators [22–24], quasi-2D spin-orbit-coupled superconductors with a perpendicular Zeeman field [25–30], and planar Josephson junctions [31–37], etc. It has been a challenging task to decisively confirm the existence of MZM in the various experimental systems due to other competing mechanisms that can potentially result in similar features as MZM do in different probes [34, 35, 38–43]. Other proposals for constructing Kitaev chains through a bottom-up approach, based on, e.g. magnetic tunnel junctions proximate to spin-orbit-coupled superconductors [44], and quantum dots coupled through superconducting links [45–47] are therefore promising. In particular, the recent experiment [47] of a designer minimal Kitaev chain based on two quantum dots coupled through tunable crossed Andreev

reflections (CAR) offers a compelling route towards MZM platforms based on exactly solvable building blocks.

In parallel with the above efforts of realizing MZM in different materials systems, scalable architectures for quantum logic circuits based on MZM have also been intensely studied over the past decades. A major proposal among these studies is to build networks of T-junctions, which are minimal units for swapping a pair of MZM hosted at different ends of a junction, that allow braiding-based TQC [5]. Alternatively, networks based on coupled wires forming the so-called tetrons and hexons, aiming at measurement-based logic gate operations [48], have also been extensively investigated. To counter the technical challenges of engineering networks with physical wires or atomic chains, various ideas based on effective Kitaev chains, such as quasi-1D systems in thin films [49], cross Josephson junctions [37], scissor cuts on a quantum anomalous Hall insulator [24], and rings of magnetic atoms [50], etc. have been proposed. However, due to the same difficulty of obtaining or identifying genuine MZM in quasi-1D systems mentioned above, it remains unclear how practical these strategies are in the near future.

In this Letter, we propose an alternative structural unit for manipulating MZM, triangular superconducting islands, motivated by the above challenges associated with wire geometries and by the fact that triangular islands routinely appear spontaneously in epitaxial growth [51] on close-packed atomic surfaces. We first show that a minimal "Kitaev triangle" consisting of three sites hosts MZM at different pairs of vertices controlled by Peierls phases on the three edges [Fig. 2.1 (a)], which can be readily realized using quantum dots. To generalize the minimal model to triangular structures involving more degrees of freedom, we study the topological phase transitions of quasi-1D ribbons driven by Peierls phases, which can be created by magnetic fields or supercurrents [52, 53], and use the resulting phase diagram as a guide to construct finite-size triangles with a hollow interior that host MZM [Fig. 2.1 (b)]. In the end we discuss possible experimental systems that can realize our proposals and scaled-up networks of triangles for implementing braiding operations of MZM.

2.2 Kitaev Triangle

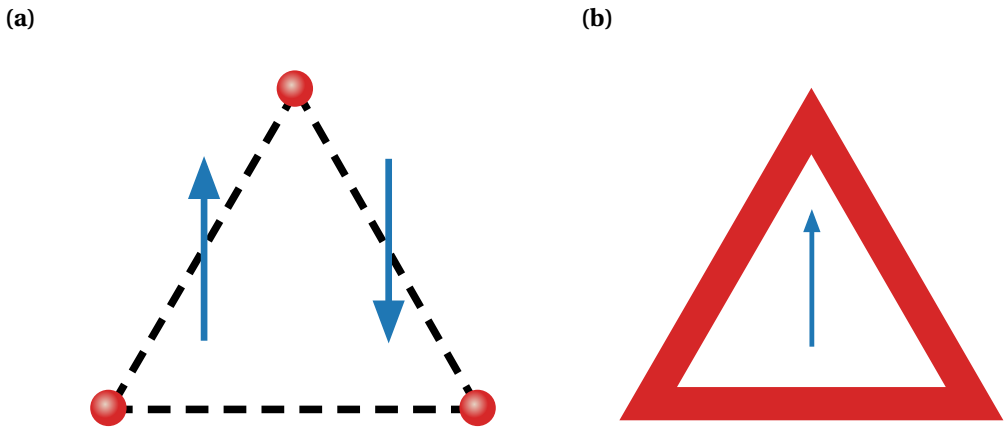

Figure 2.1: Schematics of two triangle structures proposed in this work. (a) Three-site Kitaev triangle with bond-dependent Peierls phases. (b) Hollow triangular island with a uniform vector potential.

In this section we present an exactly solvable minimal model with three sites forming a "Kitaev triangle" that can host MZM at different pairs of vertices controlled by Peierls phases on the edges. The Bogoliubov-de Gennes (BdG) Hamiltonian includes complex hopping and p-wave pairing between three spinless fermions forming an equilateral triangle [Fig. 2.1 (a)]:

$$\mathscr{H} = \sum_{\langle jl \rangle} (-te^{i\phi_{jl}} c_j^\dagger c_l + \Delta e^{i\theta_{jl}} c_j c_l + \text{h.c.}) - \sum_j \mu c_j^\dagger c_j, \tag{2.1}$$

where t is the hopping amplitude, Δ is the amplitude of the (2D) p-wave pairing, μ is the chemical potential, θ_{jl} is the polar angle of $\mathbf{r}_{jl} = \mathbf{r}_l - \mathbf{r}_j$ (the x axis is chosen to be along $\mathbf{r}_{12}$), consistent with $\{c_l^\dagger, c_j^\dagger\} = 0$. ϕ_{jl} is the Peierls phase due to a bond-dependent vector potential $\mathbf{A}$ to be specified below (the nearest neighbor distance a is chosen to be the length unit hereinbelow):

$$\phi_{jl} = \frac{e}{\hbar} \int_{\mathbf{r}_j}^{\mathbf{r}_l} \mathbf{A} \cdot d\mathbf{l} = -\phi_{lj} \tag{2.2}$$

where $e>0$ is the absolute value of the electron charge. Below we use the natural units $e=\hbar=1$. To get the conditions for having MZM in this model we rewrite $\mathscr{H}$ in the Majorana fermion basis $a_j = c_j + c_j^\dagger$, $b_j = \frac{1}{i}(c_j - c_j^\dagger)$:

$$\begin{aligned}\mathscr{H} = -\frac{i}{2}\sum_{\langle jl\rangle}\Big[&\left(t\sin\phi_{jl} - \Delta\sin\theta_{jl}\right)a_j a_l \\ &+\left(t\sin\phi_{jl} + \Delta\sin\theta_{jl}\right)b_j b_l \\ &+\left(t\cos\phi_{jl} - \Delta\cos\theta_{jl}\right)a_j b_l \\ &-\left(t\cos\phi_{jl} + \Delta\cos\theta_{jl}\right)b_j a_l\Big] - \frac{i\mu}{2}\sum_j a_j b_j\end{aligned} \tag{2.3}$$

For concreteness we consider the Kitaev limit $t=\Delta$, $\mu=0$, and choose $\phi_{12}=0$ so that sites 1 and 2 alone form a minimal Kitaev chain with $\mathscr{H}_{12} = i\,t\,b_1 a_2$ and hosting MZM a_1 and b_2. In order for the MZM to persist in the presence of site 3, one can choose ϕ_{23} and ϕ_{31} so that all terms involving these Majorana operators cancel out. For example, consider the $2-3$ bond, for which $\theta_{23} = 2\pi/3$, we require

$$\sin\phi_{23} + \sin\frac{2\pi}{3} = \cos\phi_{23} + \cos\frac{2\pi}{3} = 0 \tag{2.4}$$

which means $\phi_{23} = -\pi/3$. Similarly one can find $\phi_{31} = -\phi_{13} = -\pi/3$. The three Peierls phases can be realized by the following staggered vector potential

$$\mathbf{A} = [1 - 2\Theta(x)]\,\frac{2\pi}{3\sqrt{3}}\mathbf{y} \tag{2.5}$$

where $\Theta(x)$ is the Heavisde step function. In fact, using a uniform $\mathbf{A} = \frac{2\pi}{3\sqrt{3}}\mathbf{y}$, which corresponds to $\phi_{23} = -\pi/3 = -\phi_{31}$ also works, since the existence of a_1 is unaffected by ϕ_{23}. However, in this case the counterpart of b_2 is not localized on a single site. For the same reason, the above condition for MZM localized at triangle corners can be generalized to Kitaev chains forming a triangular loop, as well as to finite-size triangles of 2D spinless p-wave superconductors in

the Kitaev limit, as the existence of a_1 and b_2 are only dictated by the vector potential near the corresponding corners. It should be noted that in the latter case, 1D Majorana edge states will arise when the triangle becomes larger, and effectively diminish the gap that protects the corner MZM. On the other hand, for the longer Kitaev chain, due to the potential practical difficulty of controlling further-neighbor hopping and pairing amplitudes, it is better to resort to the approach of controlling the individual topological phases of the three edges which will be detailed in the next section.

We next show that the minimal Kitaev triangle suffices to demonstrate braiding of MZM. To this end we consider a closed parameter path linearly interpolating between the following sets of values of ϕ_{jl}:

$$\begin{aligned}(\phi_{12},\phi_{23},\phi_{31}) &= \left(0,-\frac{\pi}{3},-\frac{\pi}{3}\right)\equiv \boldsymbol{\phi}_1 \\ &\to \left(-\frac{\pi}{3},-\frac{\pi}{3},0\right)\equiv \boldsymbol{\phi}_2 \\ &\to \left(-\frac{\pi}{3},0,-\frac{\pi}{3}\right)\equiv \boldsymbol{\phi}_3 \\ &\to \boldsymbol{\phi}_1\end{aligned} \tag{2.6}$$

It is straightforward to show that at $\boldsymbol{\phi}_2$ and $\boldsymbol{\phi}_3$ there are MZM located at sites $3,1$ and $2,3$, respectively. Therefore the two original MZM at sites $1,2$ should switch their positions at the end of the adiabatic evolution.

Indeed, Fig. 2.2 shows that the MZM stays at zero energy throughout the parameter path that interchanges their positions. To show that such an operation indeed realizes braiding, we explicitly calculated the many-body Berry phase of the evolution [4, 50, 54] and found the two degenerate many-body ground states acquire a $\frac{\pi}{2}$ difference in their Berry phases as expected [4]. Compared to the minimum T-junction model with four sites [4], our Kitaev triangle model only requires three sites to achieve braiding between two MZM, and is potentially also easier

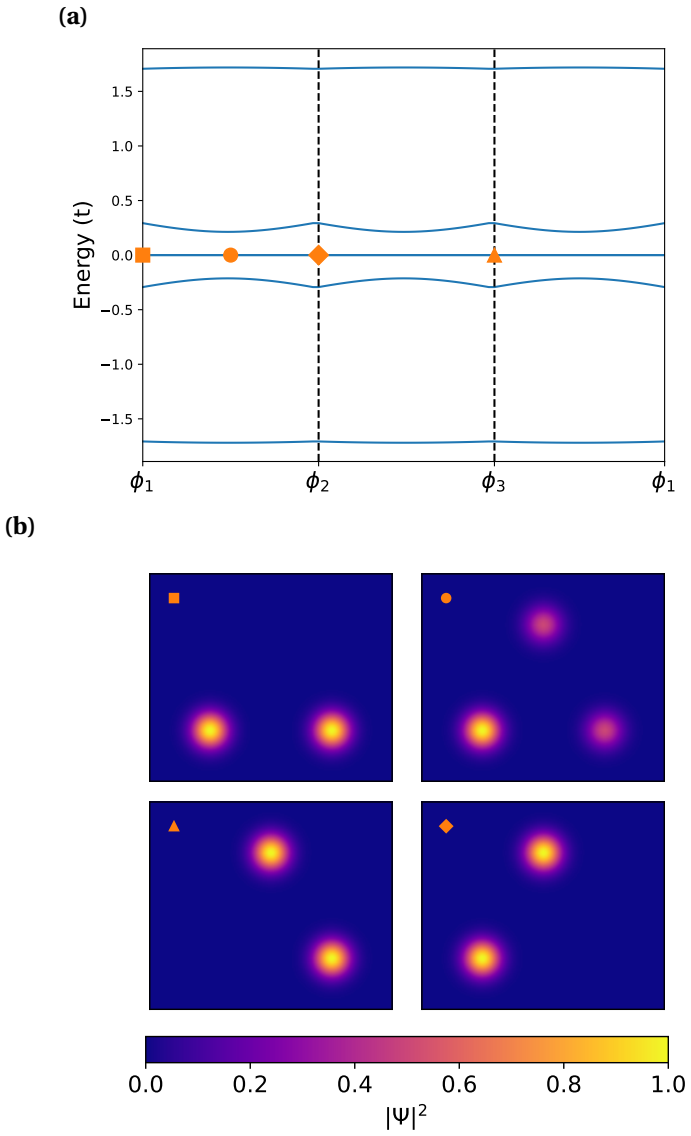

Figure 2.2: (a) Evolution of the eigenvalues of the 3-site Kitaev triangle along the closed parameter path for ϕ on the three edges. (b) MZM wavefunctions at different points of the parameter path. Clockwise from the upper left panel: $\boldsymbol{\phi}_1 \to \frac{1}{2}(\boldsymbol{\phi}_1 + \boldsymbol{\phi}_2) \to \boldsymbol{\phi}_2 \to \boldsymbol{\phi}_3$.

to engineer experimentally. In the next section we will show that a more mesoscopic hollow-triangle structure can achieve similar results and may be preferred in other materials platforms.

2.3 Hollow Triangles

For systems with less fine-tuned Hamiltonians than the minimal model in the previous section, it is more instructive to search for MZM based on topological arguments. In this section

we show that MZM generally appear at the corners of a hollow triangle, which can be approximated by joining three finite-width chains or ribbons whose bulk topology is individually tuned by the same uniform vector potential.

To this end, we first show that topological phase transitions can be induced by a vector potential in a spinless p-wave superconductor ribbon. In comparison with similar previous proposals that mostly focused on vector potentials or supercurrents flowing along the chain [52,53], we consider in particular the tunability by varying the direction of the vector potential relative to the length direction of the ribbon, which will become instrumental in a triangular structure.

Consider Eq. (A.2) on a triangular lattice defined by unit-length lattice vectors $(\mathbf{a}_1, \mathbf{a}_2) = (\mathbf{x}, \frac{1}{2}\mathbf{x} + \frac{\sqrt{3}}{2}\mathbf{y})$ with W unit cells along $\mathbf{a}_2$ but infinite unit cells along $\mathbf{a}_1$, and assume the Peierls phases are due to a uniform vector potential $\mathbf{A}$ so that $\phi_{jl} = \mathbf{A}\cdot\mathbf{r}_{jl}$. We also introduce $\mathbf{a}_3 \equiv -\mathbf{a}_1 + \mathbf{a}_2$ for later convenience. The Hamiltonian is periodic along x and can be Fourier transformed through $c^\dagger_{m,n} = \frac{1}{\sqrt{N}}\sum_k c^\dagger_{k,n} e^{-ikm}$, where m, n label the lattice sites as $\mathbf{r}_{m,n} = m\mathbf{a}_1 + n\mathbf{a}_2$. The resulting momentum space Hamiltonian can be written as the following block form up to a constant

$$\begin{aligned} \mathscr{H} &= \frac{1}{2}\sum_k \Psi^\dagger_k \begin{pmatrix} h_t(k) & h_\Delta(k) \\ h^\dagger_\Delta(k) & -h^*_t(-k) \end{pmatrix} \Psi_k \\ &\equiv \frac{1}{2}\sum_k \Psi^\dagger_k H(k) \Psi_k \end{aligned} \tag{2.7}$$

where $\Psi_k \equiv (c_{k,1}, \ldots, c_{k,W}, c^\dagger_{-k,1}, \ldots c^\dagger_{-k,W})^T$. $h_t(k)$ is a $W \times W$ Hermitian tridiagonal matrix with $(h_t)_{n,n} = -2t\cos(k + \mathbf{A}\cdot\mathbf{a}_1) - \mu$ and $(h_t)_{n,n+1} = -t\left(e^{i(-k+\mathbf{A}\cdot\mathbf{a}_3)} + e^{i\mathbf{A}\cdot\mathbf{a}_2}\right)$. $h_\Delta(k)$ is a $W \times W$ tridiagonal matrix with $(h_\Delta)_{n,n} = -2i\Delta\sin k$ and $(h_\Delta)_{n,n\pm1} = \mp\Delta\left[e^{-i(\pm k + \frac{2\pi}{3})} + e^{-i\frac{\pi}{3}}\right]$.

By transforming Eq. (2.7) to the Majorana basis using the unitary transformation:

$$U \equiv \frac{1}{\sqrt{2}} \begin{pmatrix} 1 & 1 \\ -i & i \end{pmatrix} \otimes \mathbb{I} \tag{2.8}$$

where $\mathbb{I}$ is a $W \times W$ identity matrix, and defining $A_k \equiv -iUH(k)U^\dagger$, not to be confused with the vector potential, one can calculate the Majorana number [7] $\mathscr{M}$ of the 1D ribbon as [55]

$$\mathscr{M} = \text{sgn}\left[\text{Pf}(A_{k=0})\text{Pf}(A_{k=\pi})\right] \tag{2.9}$$

where Pf stands for the Pfaffian of a skew-symmetric matrix [7]. When $\mathscr{M} = -1$, the 1D system is in a nontrivial topological phase with MZM appearing at open ends of semi-infinite ribbons, and otherwise for $\mathscr{M} = 1$.

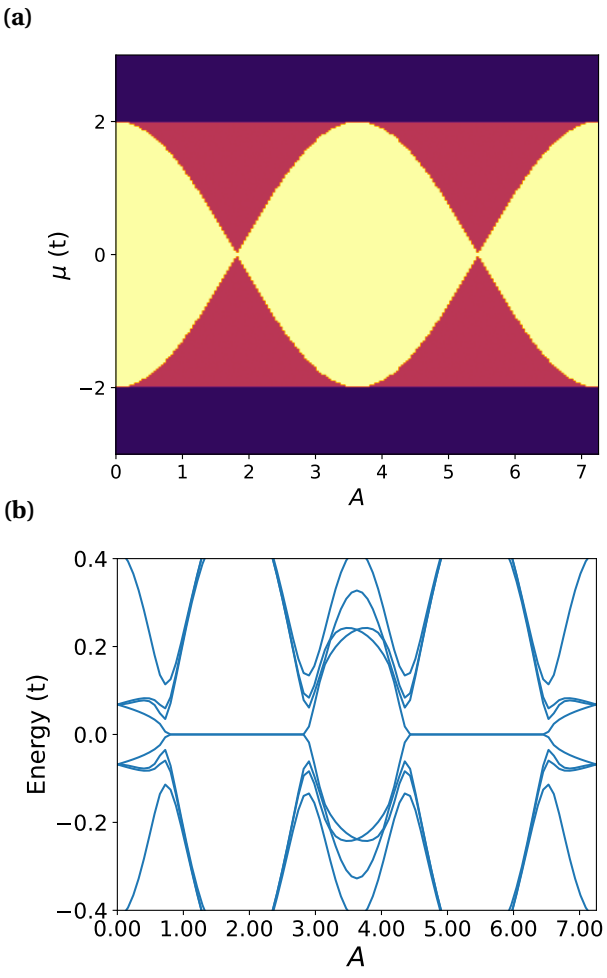

Figure 2.3: (a) Topological phase diagram for a $W = 1$ triangular chain with the Hamiltonian Eq. (2.7) obtained by superimposing the $\mathscr{M}(A,\mu)$ plots of 1D chains with $\mathbf{A} = A\mathbf{y}$ and $\mathbf{A} = A(\frac{\sqrt{3}}{2}\mathbf{x} + \frac{1}{2}\mathbf{y})$. Color scheme: white—$\mathscr{M} = 1$, dark blue—$\mathscr{M} = -1$, light blue—$\mathscr{M} = 0$ (b) Near-gap BdG eigen-energies vs A for a finite triangle with edge length $L = 50$, $W = 1$, and $\mu = 1.6$.

In Fig. 2.3 (a) we show the topological phase diagrams for a 1D ribbon with width $W = 1$, $\mathbf{A} = A\mathbf{y}$ and $\mathbf{A} = A(\frac{\sqrt{3}}{2}\mathbf{x} + \frac{1}{2}\mathbf{y})$ superimposed (see below). We found that the vector potential component normal to the ribbon length direction has no effect on the Majorana number, nor does the sign of its component along the ribbon length direction. However, topological phase transitions can be induced by varying the size of the vector potential component along the ribbon, consistent with previous results [52, 53]. These properties motivate us to consider the structure of a hollow triangle formed by three finite-width ribbons subject to a uniform vector potential $\mathbf{A} = A\mathbf{y}$ as illustrated in Fig. 2.1 (b). The light blue color on the phase diagram Fig. 2.3 (a) therefore means that the bottom edge and the two upper edges of the hollow triangle have different $\mathscr{M}$, which should give rise to MZM localized at the two bottom corners if the triangle is large enough so that bulk-edge correspondence holds, and gap closing does not occur at other places along its edges.

To show that corner MZM indeed appear when the conditions given by the phase diagram Fig. 2.3 (a) are met, we directly diagonalize the BdG Hamiltonian of a finite hollow triangle with edge length $L = 50$ and width $W = 1$. Fig. 2.3 (b) shows the spectral flow (BdG eigen-energies evolving with increasing vector potential A) close to zero energy at chemical potential $\mu = 1.6$. Indeed, zero-energy modes appear in the regions of μ and A consistent with the phase diagram (except when the bulk band gap is too small; see [54] for some examples.). Hollow triangles with larger larger W also have qualitatively similar behavior, although the phase diagrams are more complex [54]. The eigenfunctions for the zero-energy modes at $A = 2.75$ and $\mu = 1.6$ in Fig. 2.4 (b) also confirm their spatial localization at the bottom corners of the triangle.

We finally show that rotating the uniform vector potential in-plane can manipulate the positions of the MZM without hybridizing them with bulk states for certain ranges of μ and A. Fig. 2.4 (a) plots the spectral flow versus the in-plane azimuthal angle of $\mathbf{A}$, which clearly shows that the zero-energy modes persist throughout the rotation and the bulk gap never closes. Figs. 2.4 (b-d) plot the BdG wavefunctions of the MZM at special values of φ. One can see that the two MZM appear to cycle through the three vertices by following the rotation of $\mathbf{A}$. The robustness

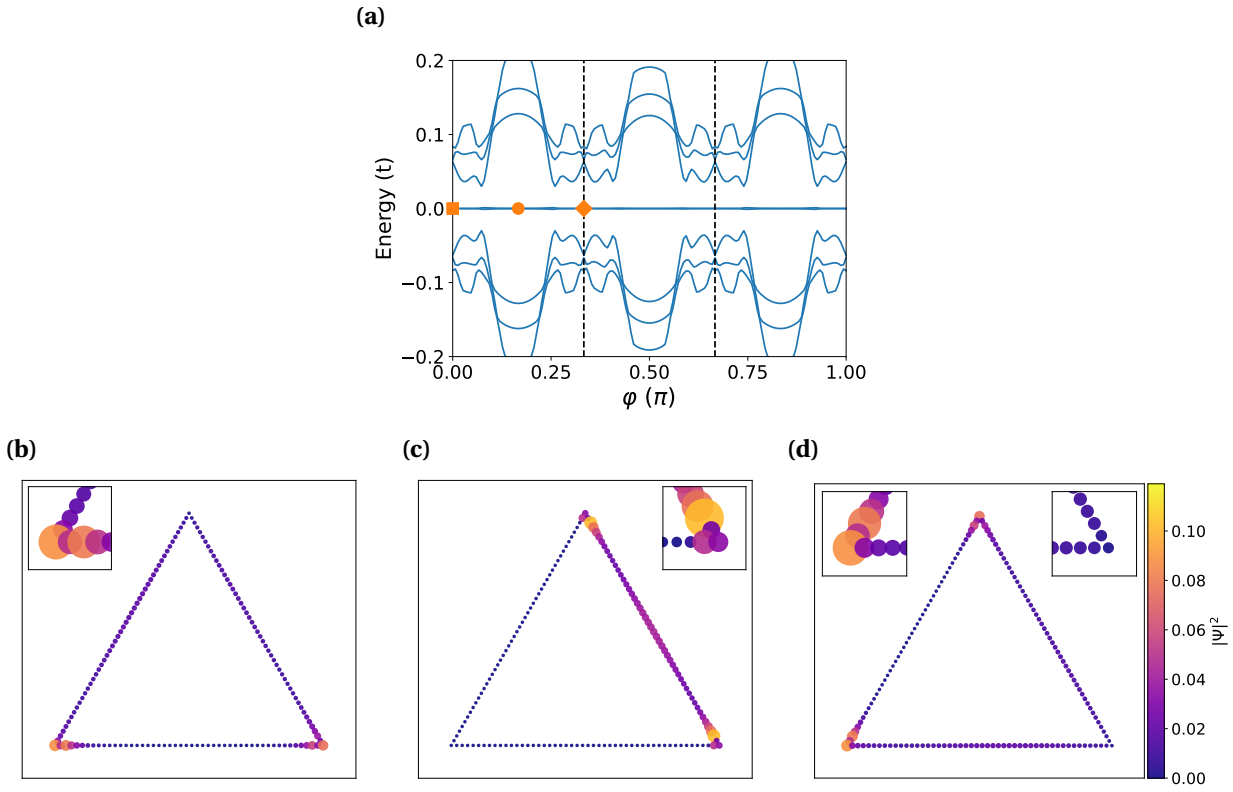

Figure 2.4: (a) Spectral flow of a hollow triangle with $W = 1$, $L = 50$, $\mu = 1.6$, and $A = 2.75$ with increasing rotation angle φ, defined through $\mathbf{A} = A(-\sin\varphi\mathbf{x} + \cos\varphi\mathbf{y})$. (b-d) BdG eigenfunction $|\Psi|^2$ summed over the two zero modes at $\varphi = 0, \frac{\pi}{6}$, and $\frac{\pi}{3}$, respectively.

of the MZM therefore requires the condition of two edges being in a different topological phase from the third one to be satisfied throughout the rotation. Such a criterion combined with the individual phase diagrams of the edges can help isolate the desired parameter regions of μ and A. We also note that the positions of the MZM do not interchange after φ increases from 0 to π, different from the situation of the minimal Kitaev triangle in Fig. 2.2. The reason is that the MZM in the latter case are not due to bulk-boundary correspondence [the values of $A = \frac{2\pi}{3\sqrt{3}}$ and $\mu = 0$ are a critical point in the phase diagram Fig. 2.3 (a)]. While the positions of the MZM at special points along the parameter path in the hollow triangle case have to be additionally constrained by the bulk topological phases of the three edges, that for the Kitaev triangle have more flexibility and are also protected by the finite size of the system.

A model that is closer to a realistic hollow triangular island is the finite-width triangular chain or ribbon. An example, illustrated in Figure 2.5 (c), has its edge length $L = 50$ and width

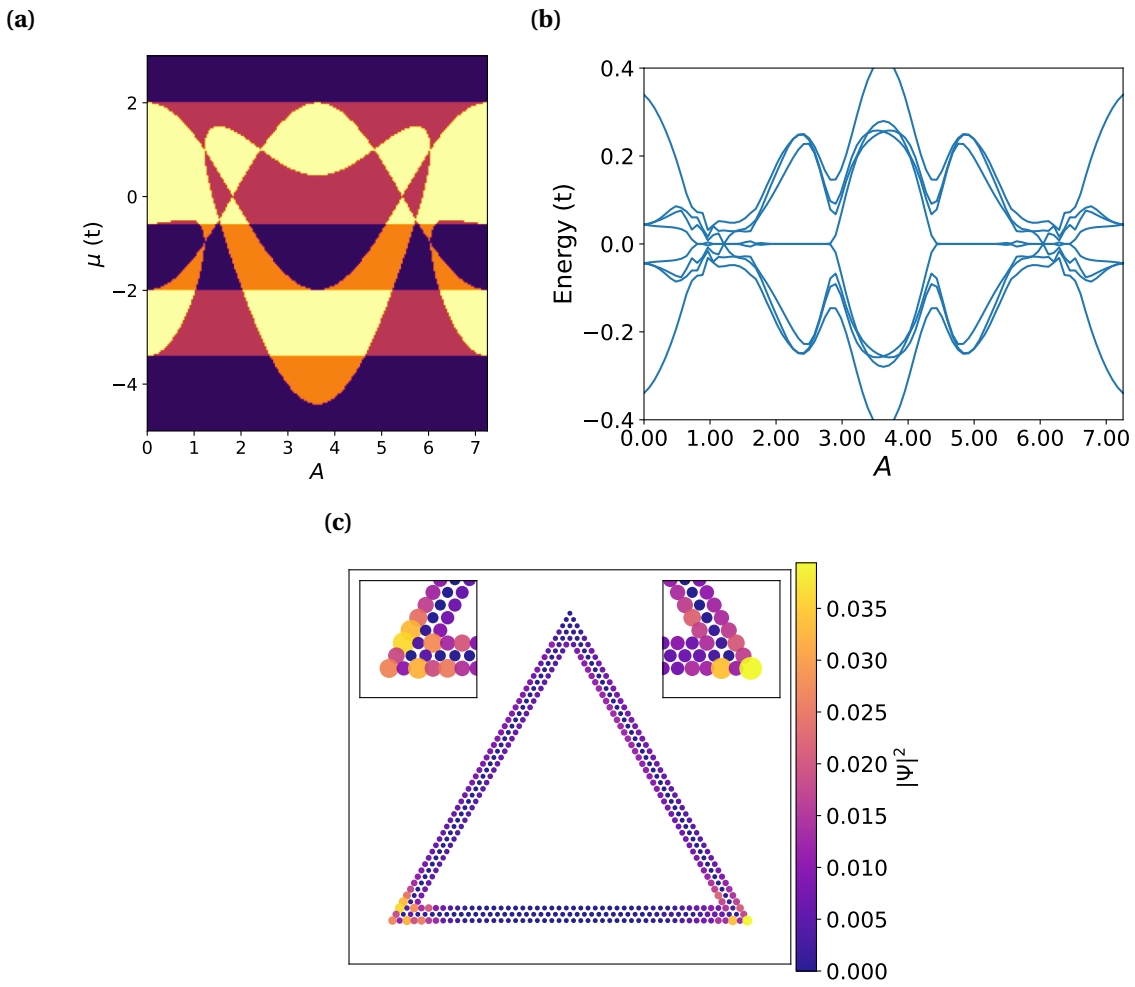

Figure 2.5: (a) Topological phase diagram for a $W = 3$ hollow triangle obtained by overlapping the $\mathscr{M}(A,\mu)$ plots of 1D chains with $\mathbf{A} = A\mathbf{y}$ and $\mathbf{A} = A(\frac{\sqrt{3}}{2}\mathbf{x} + \frac{1}{2}\mathbf{y})$. Color scheme: white—$\mathscr{M} = 1$, dark blue—$\mathscr{M} = -1$, light blue—$\mathscr{M} = 0$ (b) Near-gap BdG eigen-energies vs A for a finite triangle with edge length $L = 50$, $W = 3$, and $\mu = 1.6$. (c) BdG eigenfunction $|\Psi|^2$ summed over the two zero modes at $A = 2.4709$.

$W = 3$. The phase diagram Fig. 2.5 (a) is created in a similar way as that in Fig. 2.3 (a), assuming a constant vector potential and infinitely long $W = 3$ ribbons. The spectral flow for the actual triangle with $\mu = 1.6$ in Fig. 2.5 (b) shows MZM in the parameter regions in agreement with the phase diagram. Fig. 2.5 (c) plots the MZM wavefunction for $A = 2.7409$ and $\mu = 1.6$ that are indeed well localized at the bottom corners.

We next rotate the uniform vector potential to examine how the MZM move on a hollow triangle. Figure 2.6 shows the spectral flow and eigenfunctions as we rotate $\varphi = 0$ to $\varphi = \pi$ counterclockwisely. The two MZM cycle through the three vertices in a similar manner as that

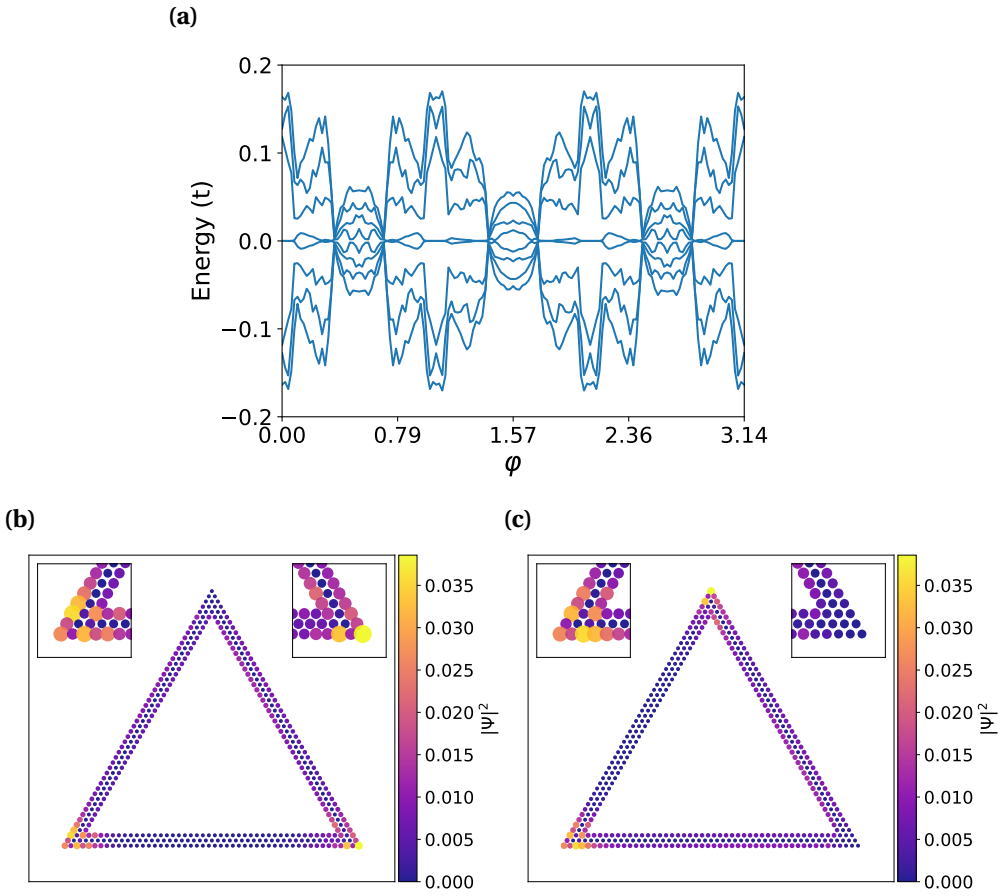

Figure 2.6: (a) Spectral flow of a hollow triangle with $W = 3$, $L = 50$, $\mu = 1.6$, and $A = 2.75$ with increasing rotation angle φ, defined through $\mathbf{A} = A(-\sin\varphi\mathbf{x} + \cos\varphi\mathbf{y})$. (b-c) BdG eigenfunction $|\Psi|^2$ summed over the two zero modes at $\varphi = 0$ and $\frac{\pi}{3}$, respectively.

in Fig. 4 of the main text (only the MZM wavefunctions at $\varphi = 0$ and $\frac{\pi}{3}$ are plotted as representatives of the $\varphi = n\pi/3$ cases). Note that the spectral flow has 3-fold rotation symmetry but not 6-fold, since increasing φ by $\frac{2\pi}{3}$ is equivalent to rotating the coordinate system clockwisely by $\frac{2\pi}{3}$. In contrast, rotating the vector potential by $\frac{\pi}{3}$, if without an additional sign change of the p-wave pairing potential, is not an exact symmetry of the finite triangle. Also we did not try to scrutinize the phase diagram to find a parameter path in which the bulk gap does not close, as in the $W = 1$ case in the main text. Here we just point out that identifying a system-specific parameter path for adiabatic manipulation of MZM is in principle always possible, especially if one is allowed to have more knobs other than φ in real structures, such as tuning the chemical potential of individual edges or the size of the vector potential, etc.

2.4 Braiding MZM in a small network of triangles

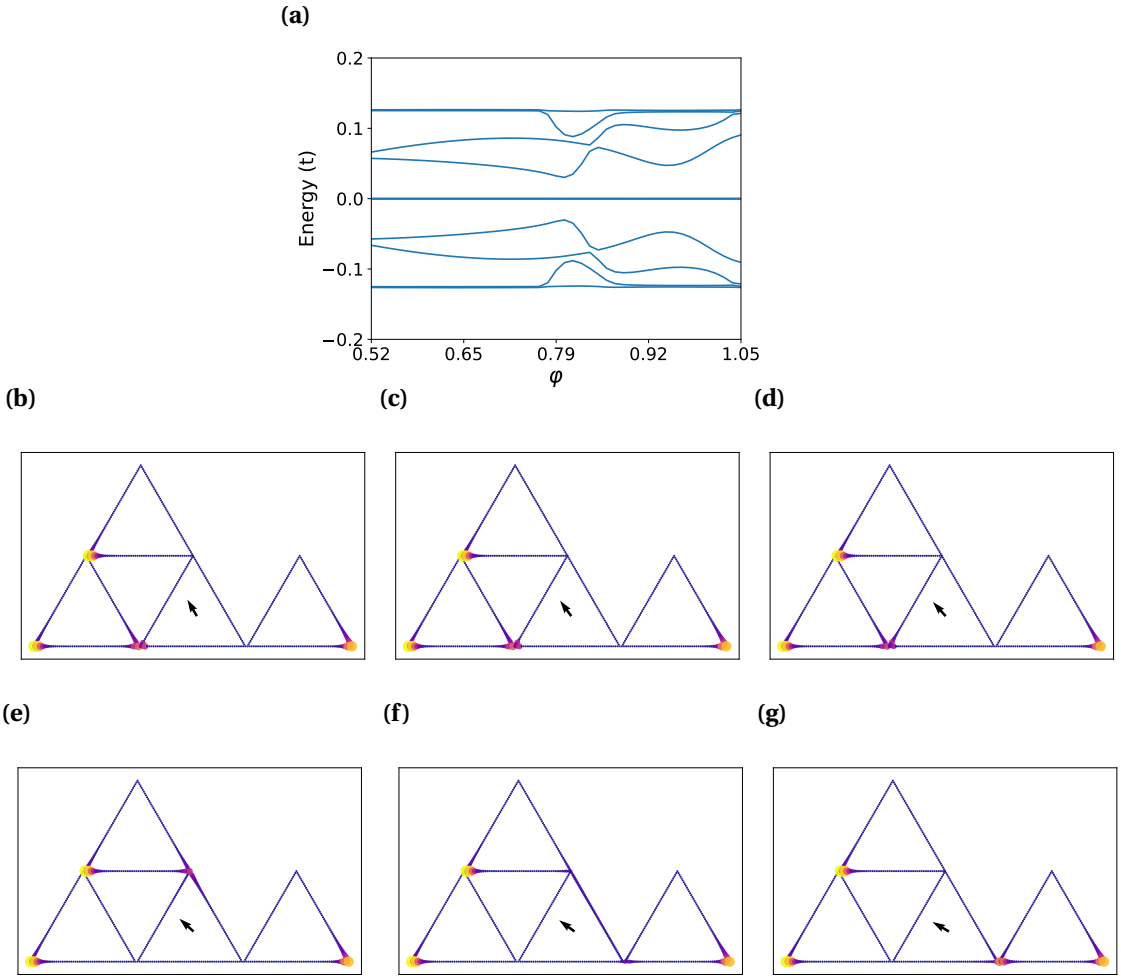

Figure 2.7: (a) Spectral flow for the critical step of swapping γ_2 and γ_3 in the example of Fig. 5 in the main text, calculated using four corner-sharing triangles of $W = 1$ and $L = 50$, with $\mu = 1.6$ and $A = 2.6$. Vector potential for the middle triangle in the bottom row can rotate according to $\mathbf{A} = A(-\sin\varphi\mathbf{x} + \cos\varphi\mathbf{y})$ from $\varphi = \frac{\pi}{6}$ to $\frac{\pi}{3}$, while the other three have fixed $\varphi = 0$. (b)-(g) BdG eigenfunction $|\Psi|^2$ summed over the four zero modes at equally-spaced points along the rotation path. The black arrow indicates the direction of the vector potential for the bottom middle triangle.

In this section we show that one can braid two out of four MZM, a minimal setting for non-trivial manipulation of the degenerate many-body ground states, by using a small network of corner-sharing triangles. We focus on the critical step of swapping γ_2 and γ_3 as labeled in Fig. 5 of the main text. This can be done by rotating the vector potential of the triangle in the middle of the bottom row from $\varphi = \frac{\pi}{6}$ to $\frac{\pi}{3}$. More specifically, when $\varphi = \frac{\pi}{6}$, with the chosen values of μ

and A, only the right edge of the said triangle is topologically nontrivial. The chain that hosts $\gamma_{3,4}$ thus extends through this nontrivial edge to the top triangle as in Fig. 2.7 (b). On the other hand, when φ increases to $\frac{\pi}{3}$, the nontrivial edge of the middle triangle changes from right to left, which leads to γ_2 hopping from its left corner to the right through the top corner, while γ_3 is unaffected [Figs. 2.7 (c-g)]. As a result the γ_2, γ_3 swapping is done without closing the bulk gap, as can be seen from the spectral flow in Fig. 2.7 (a).

2.5 Additional results using inhomogeneous vector fields

While we have showed a constant vector field works to induce and manipulate MZM for a triangular chain and hollow triangle it remains to be seen if inhomogeneous vector potential fields can repoduce the same results. We expect this to be the case due to the topological phase diagram seen in 2.3 (a) and 2.5 (a) and the results that followed for a constant vector potential.

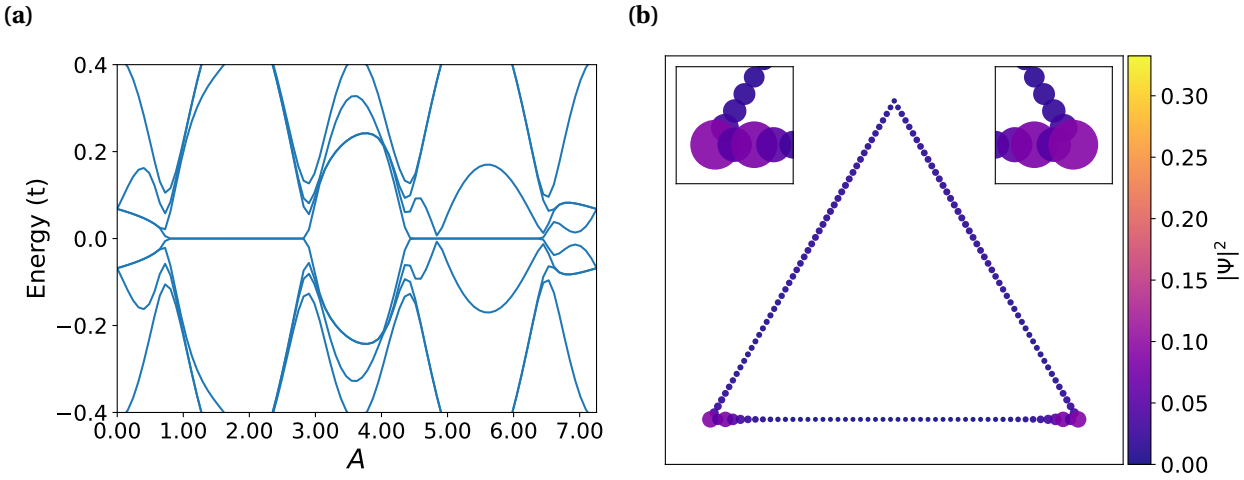

Figure 2.8: (a) Spectral flow of a hollow triangle with $W = 1$, $L = 50$, and $\mu = 1.6$ for increasing heaviside vector potential strength defined by $\mathbf{A} = A[1 - 2\Theta(x)]\mathbf{y}$ (b) BdG eigenfunction $|\Psi|^2$ summed over the two zero modes at $A = 2.7409$.

For hollow triangle of width, $W = 1$ subject to a heaviside vector potential we see a similar spectral flow and MZM in Fig. 2.8 to match 2.3. If the heaviside vector potential is not so easily made in lab it may be easier to model a tanh function instead. Also, in the limit that the tanh's

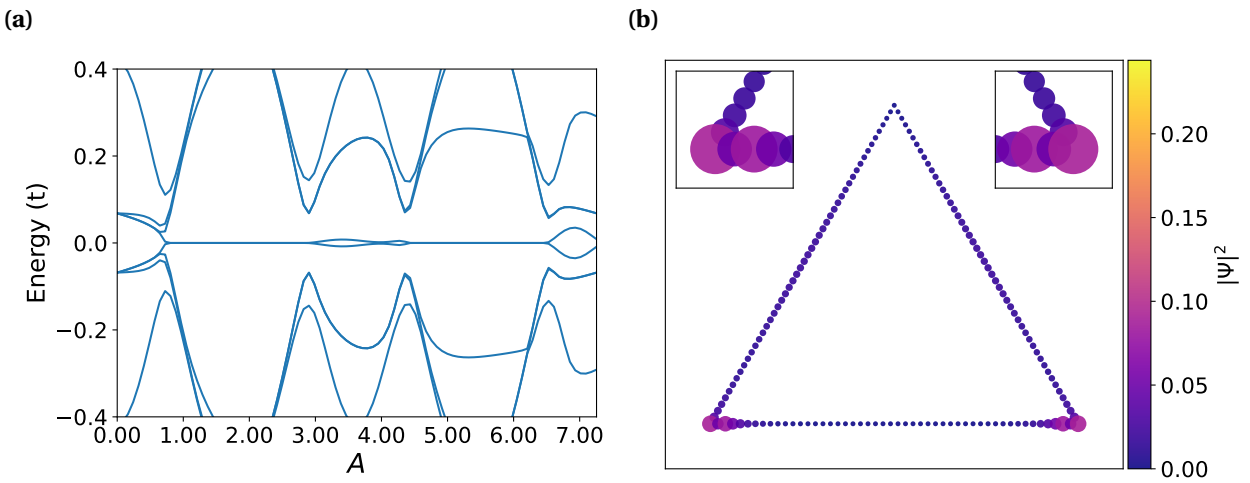

Figure 2.9: (a) Spectral flow of a hollow triangle with $W = 1$, $L = 50$, and $\mu = 1.6$ for increasing tanh vector potential strength defined by $\mathbf{A} = -A\tanh(x/2w)\mathbf{y}$, $w = a/2$ (b) BdG eigenfunction $|\Psi|^2$ summed over the two zero modes at $A = 2.7409$.

function width, w, goes to zero it is equivalent to the heaviside function. A tanh vector potential can match the same results as seen in Fig. 2.9. It should be mentioned that the width of the tanh function should be on the order or smaller than the distance between to neighboring lattice points, if two neighboring sites overall phase accumulation is not large enough to match the topological phase diagram then the bulk edge correspondence at the tanh's inflection point would cause additional MZM to appear. In other words, the top edges of the triangle should be one long bent trivial edge but if the tanh's width is too large the two edges become separated by a small non-trivial topological corner-edge because the Peierls phase is too small. Increasing the width of the hollow triangle to $W = 3$, we see similar results for heaviside, Fig. 2.10, and tanh, Fig. 2.11, compared to a constant vector potnential, Fig. 2.5.

We look at a linear vector potential next. A topological phase diagram for a linear vector potential is possible to compute, however, it requires a lattice space matrix instead of momentum space matrix due to having no periodic boundary conditions. It also requires separate calculations for longer traingular lattice ribbons. Computation times can become unruly when modeling large triangles for a high density phase diagram of A and μ values. We could, however, use the topological phase diagram in Fig. 2.3 to guess the topology for the varying Peierls phases

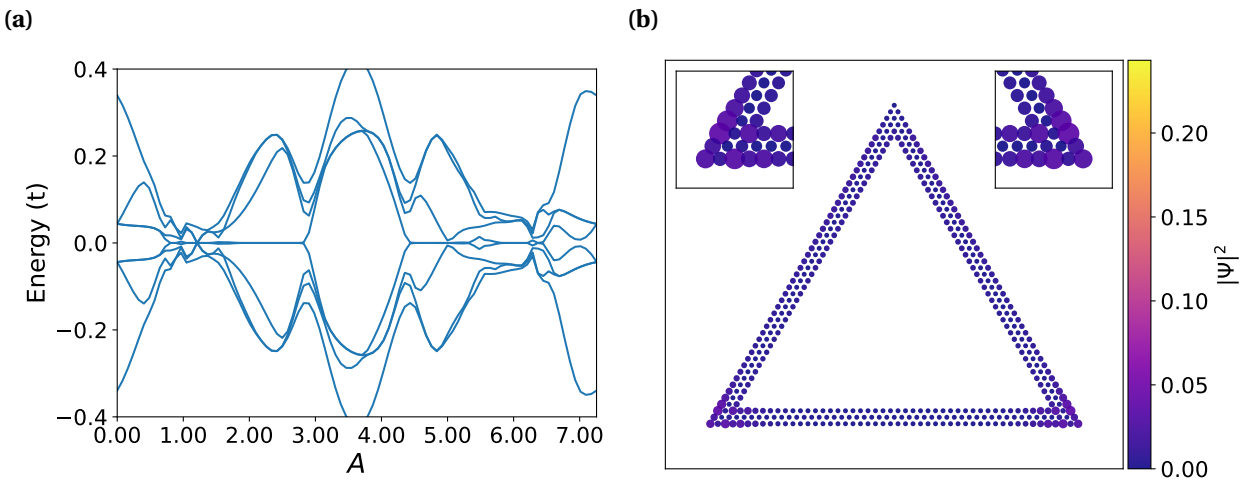

Figure 2.10: (a) Spectral flow of a hollow triangle with $W = 3$, $L = 50$, and $\mu = 1.6$ for increasing heaviside vector potential strength defined by $\mathbf{A} = A[1 - 2\Theta(x)]\mathbf{y}$ (b) BdG eigenfunction $|\Psi|^2$ summed over the two zero modes at $A = 2.7409$.

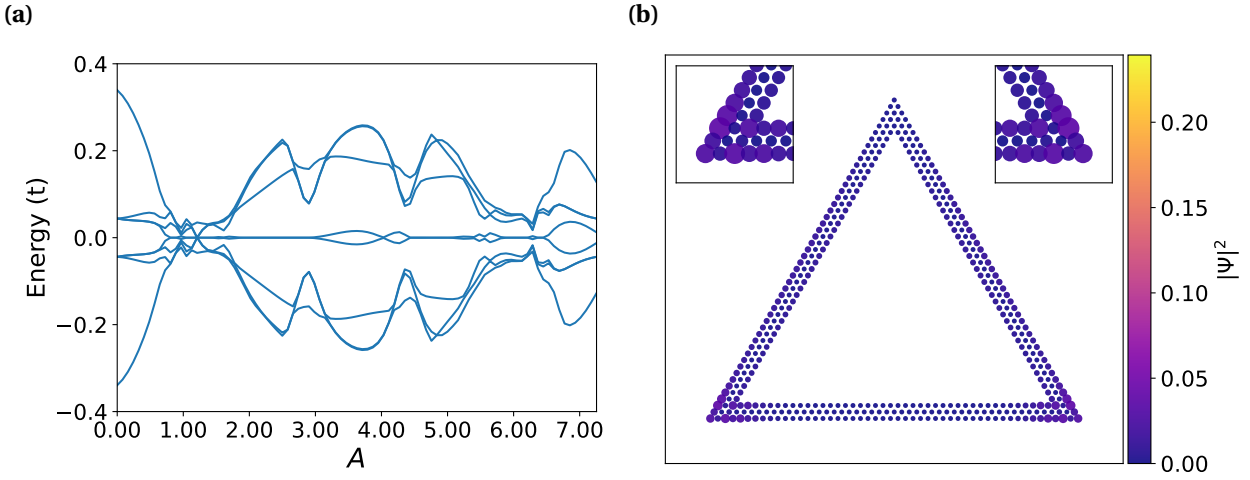

Figure 2.11: (a) Spectral flow of a hollow triangle with $W = 3$, $L = 50$, and $\mu = 1.6$ for increasing tanh vector potential strength defined by $\mathbf{A} = -A\tanh(x/2w)\mathbf{y}$, $w = a/2$ (b) BdG eigenfunction $|\Psi|^2$ summed over the two zero modes at $A = 2.7409$.

along an edge. Fig. 2.12 shows some critical points for MZMs to appear with $\mu = 0$ for a hollow triangle of $W = 1$ and $W = 3$, respectively. Fig. 2.13 shows apparent zero modes for a range of A values for a hollow triangle of $W = 1$ and $W = 3$, respectively. For similar reasons why the tanh function width needs to be small, it may be difficult to have the upper parts of the triangles top edges be all trivial topology, a small section may centered on the top corner may be non-trivial, thus hosting additional MZMs, as seen in Fig. 2.13 (c-d) half way up the triangles.

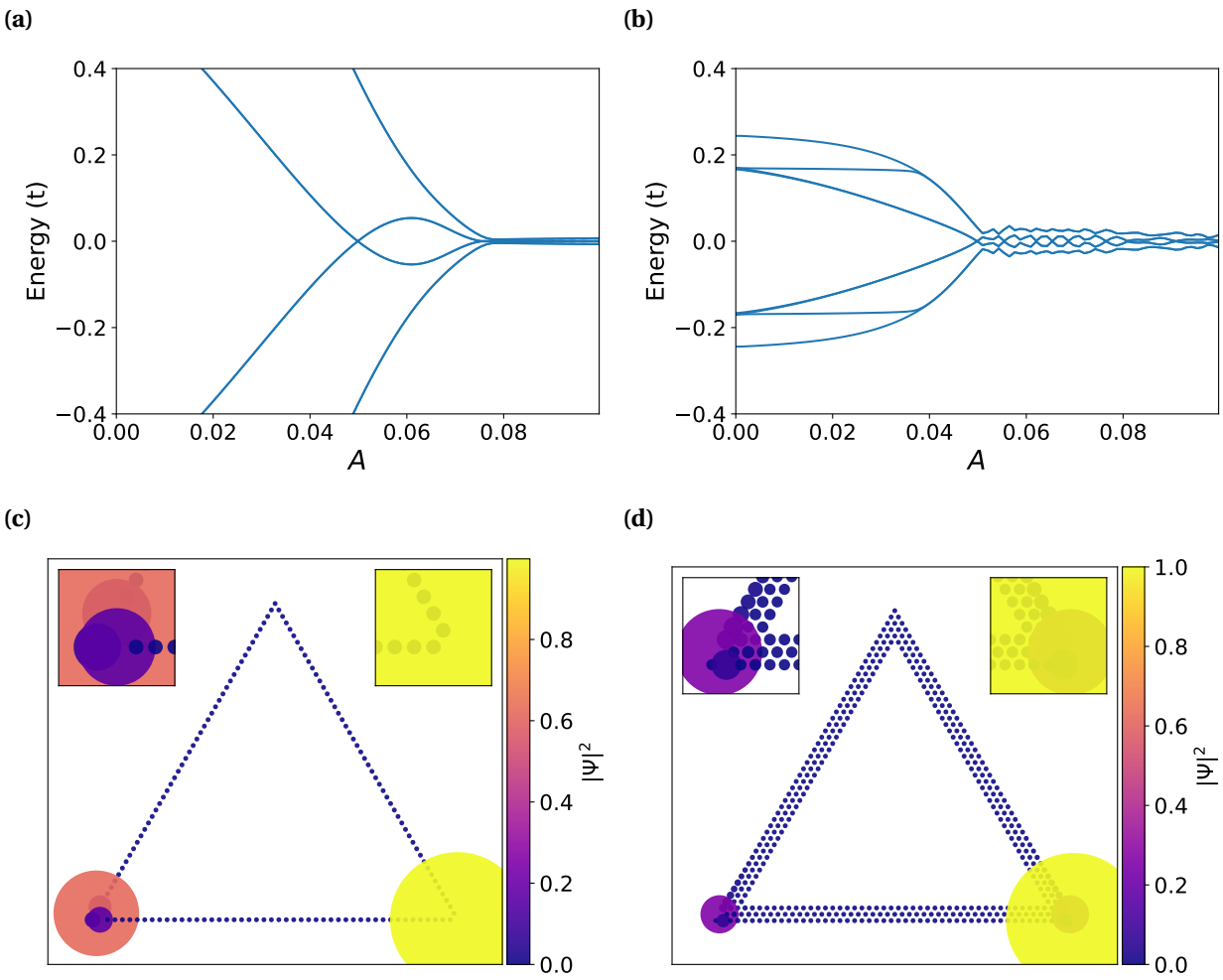

Figure 2.12: Spectral flow of a hollow triangle with $L = 50$, and $\mu = 0$ for increasing linear vector potential strength defined by $\mathbf{A} = -Ax\mathbf{y}$ (a) $W = 1$ and (b) $W = 3$ (c-d) Wavefunctions of the MZM at $A = 0.0499$ for both widths, respectively.

2.6 Discussion

The hollow interior of the triangles considered in this work is needed for two reasons: (1) $W \ll L$ is required for bulk-edge correspondence based on 1D topology to hold; (2) A finite W is needed to gap out the chiral edge states of a 2D spinless p-wave superconductor based on which Eq. (2.7) is written. The latter is not essential if one does not start with a spinless p-wave supercondutor but a more realistic model such as the Rashba+Zeeman+s-wave pairing model. On the other hand, the former constraint may also be removed if one uses the Kitaev triangle. Nonetheless, an effective 3-site Kitaev triangle may emerge as the effective theory of triangular

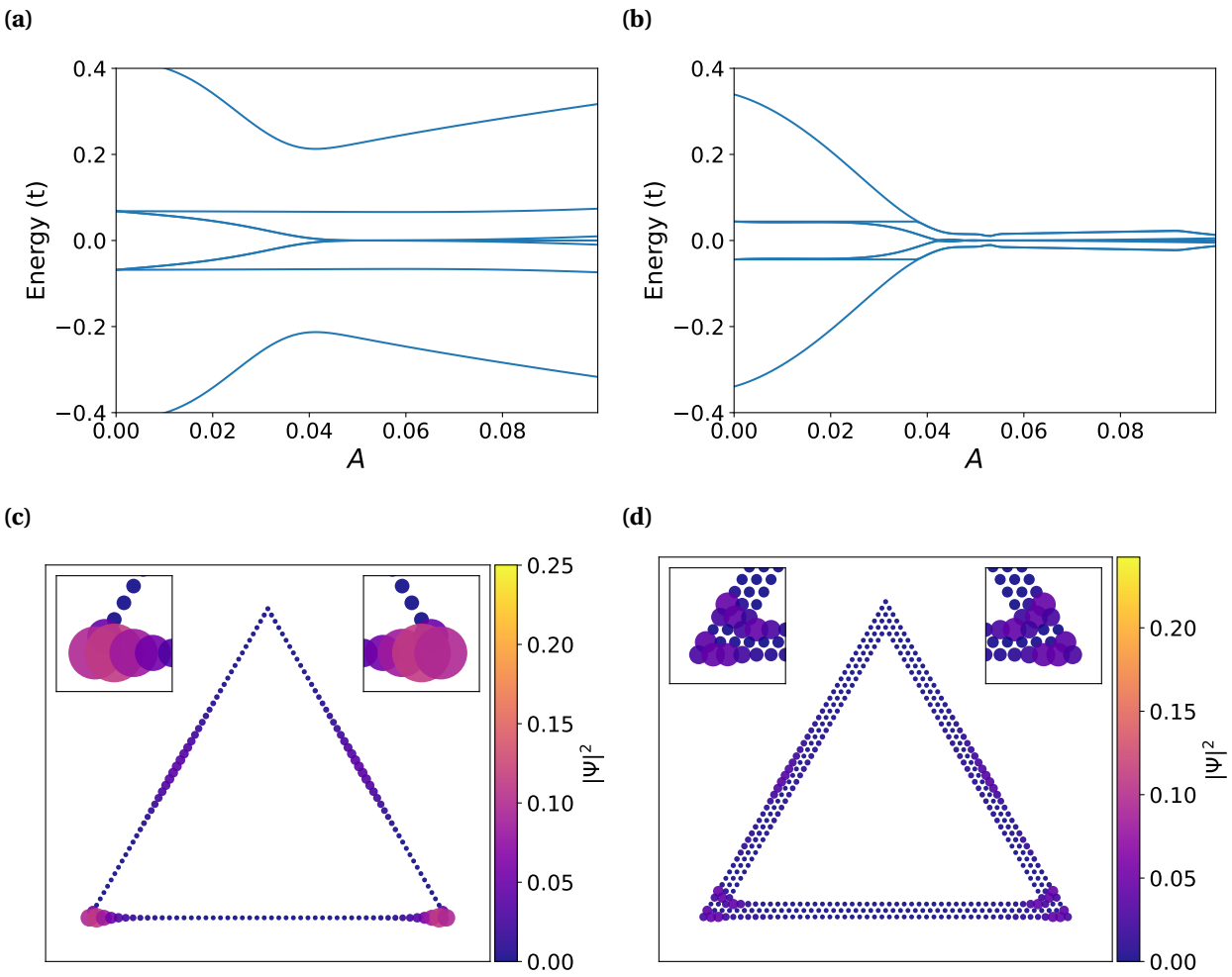

Figure 2.13: Spectral flow of a hollow triangle with $L = 50$, and $\mu = 1.6$ for increasing linear vector potential strength defined by $\mathbf{A} = -Ax\mathbf{y}$ (a) $W = 1$ and (b) $W = 3$. (c-d) Wavefunctions of the MZM at $A = 0.0598$ for both widths, respectively.

structures if a three-orbital low-energy Wannier basis can be isolated, similar to the continuum theory of moiré structures. We also note in passing that the corner MZM in our triangles appear due to different reasons from that in higher-order topological superconductors [41, 56].

For possible physical realizations of our triangles, immediate choices are quantum dots forming a Kitaev triangle [47], planar Josephson junctions or cuts on quantum anomalous Hall insulator/superconductor heterostructures [24] that form a hollow triangle, and triangular atomic chains assembled by an STM tip [17] on a close-packed surface. The quantum-dot platform may be advantageous in the convenience of implementing parity readout by turning the third

vertex temporarily into a normal quantum dot [57–59]. Looking into the future, it is more intriguing to utilize the spontaneously formed triangular islands in epitaxial growth [51] with the center region removed either physically by lithography/ablation, or electrically by gating. To create a staggered vector potential or supercurrent profile for the Kitaev triangle, one can use a uniform magnetic field, corresponding to a constant vector potential gradient, plus a uniform supercurrent that controls the position of the zero. It is also possible to use two parallel superconducting wires with counter-propagating supercurrents proximate to the triangle.

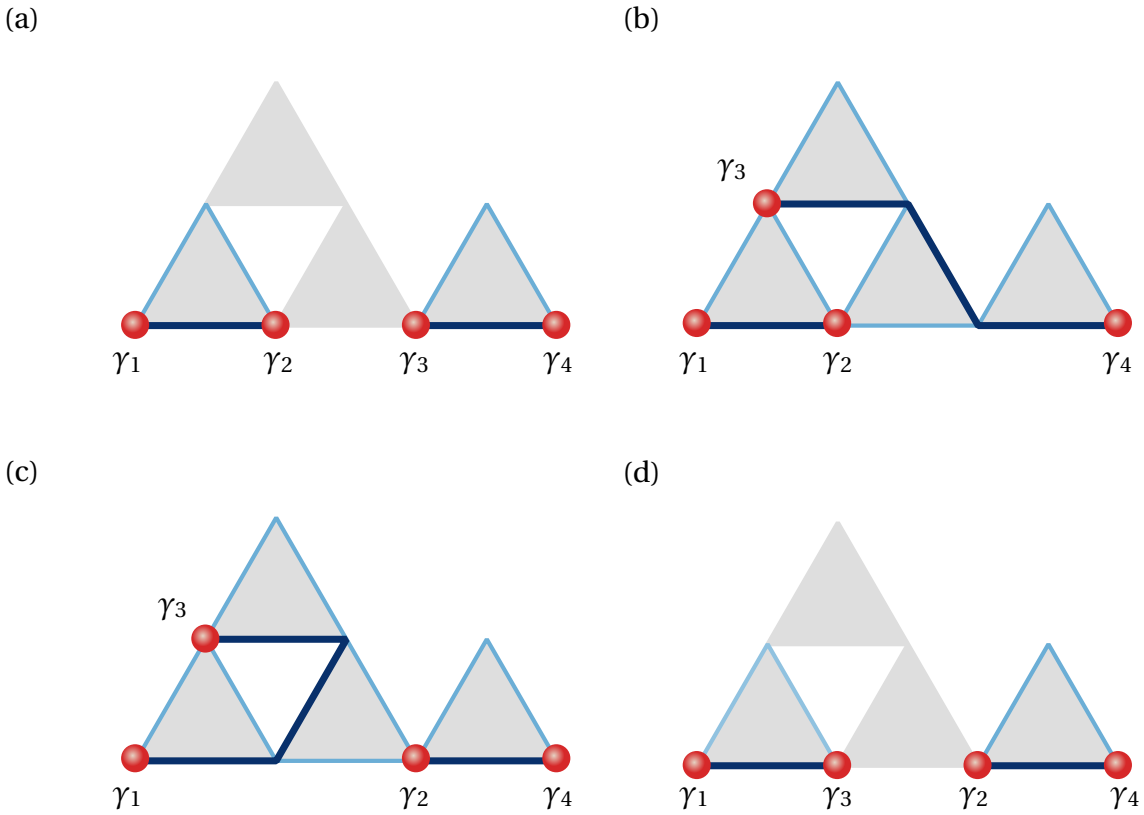

Figure 2.14: Representative steps for braiding four MZM in four triangles sharing corners. (a) Initialization of four MZM $\gamma_1, \gamma_2, \gamma_3, \gamma_4$. All three edges of the bottom-middle and the top triangles are in the trivial phase by e.g. controlling the chemical potential. The bottom-left and bottom-right triangles have $\varphi = 0$ so that their bottom edges are nontrivial. (b) Moving γ_3 by "switching on" the middle triangle by changing the chemical potential under a fixed vector potential at $\varphi = \frac{\pi}{6}$, and then turning on the top triangle with similar means except $\varphi = 0$. (c) Transporting γ_2 to the right triangle through rotating the vector potential in the middle triangle counterclockwise by $\pi/6$. (d) Moving γ_3 to the left triangle by "switching off" the top triangle followed by the middle triangle.

A tentative design for braiding more than two MZM, illustrated in Fig. 2.14, consists of four triangles sharing corners with their neighbors. The critical step of transporting γ_2 to the left vertex of the rightmost triangle, corresponding to Figs. 2.14 (b,c), can be achieved by rotating the vector potential of the bottom-middle triangle counterclockwisely from $\varphi = \frac{\pi}{6}$ to $\frac{\pi}{3}$, which swaps the topological phases of the two side edges as shown in Fig. 2.4. In [54] we show this operation does not involve gap closing at least for certain parameter regions. Our work provides a versatile platform for manipulating MZM based on currently available candidate MZM systems and for potentially demonstrating the non-Abelian nature of MZM in near-term devices.

Chapter 3

Floquet Landau Levels

3.1 Introduction

The quantum Hall effect (QHE) in conventional two-dimensional electron gas (2DEG) is one of the most remarkable phenomena in condensed matter physics [60]. This effect is indeed associated with a uniform external perpendicular magnetic field, which splits the electron energy spectrum into discrete Landau levels (LLs). Subject to a strong magnetic field, the diagonal (longitudinal) electric conductivity is vanishingly small, while the nondiagonal (Hall) conductivity is quantized. This happens due to the fact that, when the Fermi energy lies in the gap between two LLs, it is referred to as integer QHE as the Hall conductivity takes values of $2(n+1)e^2/h$ with an integer n. Recent experimental realization of graphene has stimulated additional interest to explore QHE in two dimensional systems [61–63]. Graphene exhibits unusual quantized Hall conductivity values of $2(2n+1)e^2/h$ due to application of the magnetic field [63], which are different from conventional 2DEG.

This significant effect is important to explore in Floquet systems [64, 65] because one may want to observe new phases in an alternative venue that can be experimentally realized [66–69]. Time periodically modulated Floquet theory has been extensively studied and well established for a large class of systems [65, 70–74]. Therefore, one may employ the high frequency expansions [65, 73–80] such as the well known Floquet-Magnus expansion [78–81] and Van Vleck expansion [65, 73]. The significant difference is that latter provides an explicit formulas for the time evolution operator starting at initial time $t_0 = 0$ rather than former starting with finite time t_0 [54]. In such nonequilibrium systems, a circularly polarized laser light made topology nontrivial in spite of triviality in equilibrium [82]. This nontrivial topology is similar to the quantum Anomalous Hall effect proposed by Haldane [83]. Further, optical manipulation of matter is emerging as a promising way of exploring novel phases [84, 85]. This leads to Floquet-

Bloch states exhibiting emerging physical properties that are otherwise inaccessible in equilibrium [86], i.e., the Floquet Chern insulator [87], Floquet notion of magnetic and other strongly-correlated phases [88], topological classifications, symmetry-breaking concept, and symmetry protected topological phases in nonequilibrium quantum many-body systems [88, 89]. Furthermore, it is important to note that these studies have been demonstrated in the presence of time-periodic homogeneous laser lights. However, the application of spatially inhomogeneous [90–94] laser lights have not been considered so far to best of our knowledge.

In this Letter, it is stirring to unveil that QHE can be observed in Floquet systems without need of uniform magnetic field. We show that two linearly polarized lights are an effective and versatile way of realizing QHE either in graphene-like 2D systems or in conventional 2DEG. Additionally, any one or both lights need to be spatially inhomogeneous. Employing the Floquet theory, we rely on the standard degenerate perturbation formalism and use the Van Vleck expansion [54, 65, 73]. Finally, to obtain the effective Hamiltonian and corresponding band-structure, we employ the long wavelength limit for spatially inhomogeneous modulation. We believe that our work provides a new platforms for realizing QHE and related novel phases in nonequilibrium systems.

3.2 Floquet LLs in Dirac systems

Dirac electrons can be represented with a generic model Hamiltonian like 2D graphene monolayer,

$$H^D = v_F(\sigma_x\Pi_x + \sigma_y\Pi_y), \tag{3.1}$$

where $\Pi = \mathbf{p}+e\mathbf{A^D}$, here $\mathbf{A^D}$ is the vector potential, $\mathbf{p}$ is the momentum operator, v_F is the Fermi velocity of Dirac fermions, e the absolute value of electron charge, and σ the Pauli matrices

vector in 2D. We have two linearly polarized laser lights with the electric field components

$$\mathbf{E}_1 = E\cos(\omega t)\mathbf{x},$$

$$\mathbf{E}_2 = E\sin(Kx)\sin(2\omega t)\mathbf{y}, \tag{3.2}$$

where second light is spatially inhomogeneous. It is important to note that second light need to have twice higher frequency than first. This is basic requirement to have LLs spectrum in Dirac systems. Further, one light is propagating along y-axis and polarization is along x-axis, and the other is propagating along x-axis and polarization along y-axis. The ω is frequency of light with time t, $K = 2\pi/a$ with a being the spatial period of the electric field with amplitude E. This form of the field leads ($\mathbf{E} = -\frac{\partial \mathbf{A^D}}{\partial t}$) to the following vector potential $\mathbf{A^D}$

$$\mathbf{A^D} = \left\langle -V_y \sin(\omega t), V_x \cos(2\omega t), 0 \right\rangle, \tag{3.3}$$

where we have $V_y = \frac{ev_F E}{\omega}$, $V_x = \frac{ev_F E}{2\omega}\sin(Kx)$. Substituting Eq. (3.3) into Eq. (3.1), we arrive at

$$H^D(t) = H_0^D - \sigma_x V_y \sin(\omega t) + \sigma_y V_x \cos 2(\omega t), \tag{3.4}$$

where $H_0^D = v_F(\sigma_x p_x + \sigma_y p_y)$. Because of the time-translation symmetry through $A(t+T) = A(t)$ with $T = 2\pi/\omega$, one can apply the Floquet theory [54, 65, 73] and obtain an effective Hamiltonian from Eq. (3.4). After performing the Fourier transform of the time-periodicity, first and second order expansion in $\hbar\omega$ terms leads to the final effective Hamiltonian in Eq. (3.4) as

$$H_{\text{eff}}^D = H_0^D - \frac{V_y^2 v_F \sigma_y p_y}{\hbar^2\omega^2} - \frac{V_y^2 V_x \sigma_y}{2\hbar^2\omega^2} - \frac{v_F \sigma_x (V_x^2 p_x + p_x V_x^2)}{8\hbar^2\omega^2}. \tag{3.5}$$

In Eq. (3.5), first order term in $\hbar\omega$ that leads to gap at the Dirac point in usual circularly polarized light experiments [67, 69] is zero here due to inhomogeneous nature of laser lights. This

effective Hamiltonian can be simplified in the long wavelength limit to

$$H^D_{\text{eff}} = v'_F \sigma_x p_x + v_F \sigma_y (p_y - eB^D x) \tag{3.6}$$

In obtaining Eq. (3.6), last term in Eq. (3.5) is second order in space and thus zero in the long wavelength limit for the spatially inhomogeneous modulation. Further, we have $v'_F = v_F/C, B^D = \frac{V_y^2 E}{4\hbar^2\omega^3 C}K$, with $C = 1 - V_y^2/(\hbar^2\omega^2)$. In accordance with Eqs. (3.5) and (3.6), there is least anisotropy in the Dirac spectrum in addition to zero gap. Diagonalizing the Hamiltonian in Eq. (3.6), we obtained the eigenvalues for Dirac system as

$$E^D_n = \sqrt{n(v'_F v_F B^D) 2e\hbar}, \tag{3.7}$$

which is similar to graphene LLs spectrum in the limit of equal velocities. We can have gapped Dirac spectrum by using uniform circularly polarized laser light as observed in experiments [67,69] or by using any substrate like hBN. It is also important to note that the effective magnetic field strength obtained for Dirac case in Eq. (3.7) is directly proportional to third order of the electric field and inversely proportional to the product of spatial period and fifth order of the frequency of the polarized light $\propto (E^3/(a\omega^5))$. This factor of the laser lights can be tuned and thus effective magnetic field can be enhanced in such nonequilibrium situations.

3.2.1 Dirac Numerical Approach

We now look beyond perturbation theory. In doing so we will have to solve the system numerically, which we will describe next. The incident laser light doesn't allow for translation symmetry along the x-axis for our Dirac honeycomb system. We consider a simple model using 4 atoms in a unit cell, the lattice vectors are $\mathbf{a}_1 = \sqrt{3}a\mathbf{x}$ and $\mathbf{a}_2 = 3a\mathbf{y}$, as can be seen in figure **??**. Our Hamiltonian takes the following form

$$H = -\sum_{j'l'\alpha, jl\beta} t^{j'l'\alpha}_{jl\beta} C^\dagger_{j'l'\alpha} C_{jl\beta} + h.c., \tag{3.8}$$

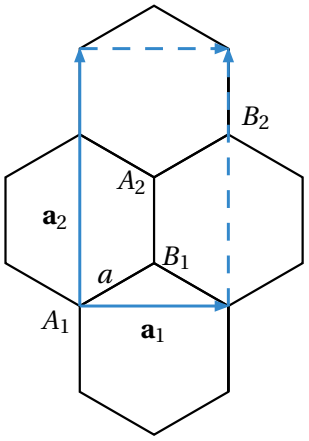

where t is the hopping amplitude, j, l are unit cell index in x and y, and $\alpha, \beta = A_1, A_2, B_1, B_2$. The vector potential is

$$\mathbf{A}(\mathbf{r}, t) = -\frac{E}{\omega}\sin(\omega t)\mathbf{x} + \frac{E}{2\omega}\sin(Kx)\cos(2\omega t)\mathbf{y}. \tag{3.9}$$

To include the vector potential in the tight-binding model we consider a finite system defined by $r_c \geq \max(|x_{i\alpha}|, |y_{i\beta}|)$. Using a Peierls substitution we can write the hopping term as

$$\begin{aligned} t_{jl\beta}^{j'l'\alpha} &= \exp\left[i\phi_0 \left\{ (x_{j'l'}^{\alpha} - x_{jl}^{\beta})\sin\omega t - \frac{1}{2}\sin\left(K\frac{x_{j'l'}^{\alpha} + x_{jl}^{\beta}}{2} \right)(y_{j'l'}^{\alpha} - y_{jl}^{\beta})\cos 2\omega t \right\} \right] \\ &= \exp\left[iX_1\sin(\omega t) - iX_2\cos(2\omega t) \right] \end{aligned} \tag{3.10}$$

where $t = 1$ and $\phi_0 = \frac{eEa}{\hbar\omega}$. One can fourier transform along the y-axis to momentum space to simplify our system to

$$H = -\sum_{jk}\left[\Psi_{jk}^{\dagger} H_{j,j} \Psi_{jk} + \Psi_{j+1,k}^{\dagger} H'_{j+1,j,k} \Psi_{jk} + h.c. \right], \tag{3.11}$$

where $\Psi_{jk} = [C_{jkA_1}, C_{jkB_1}, C_{jkA_2}, C_{jkB_2}]^T$. The two matrices are

$$H_{j,j} = \begin{bmatrix} 0 & t_{jlB_1}^{jlA_1} & 0 & 0 \\ 0 & 0 & t_{jlA_2}^{jlB_1} & 0 \\ 0 & 0 & 0 & t_{jlB_2}^{jlA_2} \\ 0 & 0 & 0 & 0 \end{bmatrix}$$

and

$$H'_{j+1,j,k} = \begin{bmatrix} 0 & t_{jlB_1}^{j+1,lA_1} & 0 & t_{jlB_2}^{j+1,l+1,A_1} e^{i\mathbf{k}\cdot\mathbf{a}_2} \\ 0 & 0 & 0 & 0 \\ 0 & 0 & 0 & t_{jlB_2}^{j+1,lA_2} \\ 0 & 0 & 0 & 0 \end{bmatrix},$$

where $\mathbf{k} = k\mathbf{y}$. The Hamiltonian dimension is reduced to $N_S \times N_S$, with $N_S = 2r_c + 1$.

For Floquet theorem we next consider how to construct the Quasienergy operator $\bar{Q}$. We first need to calculate the fourier time transform of our Hamiltonian. Each component of the matrix can be written as the following

$$\begin{aligned} H_{ab,n} &= \frac{1}{T}\int_0^T H_{ab} e^{-in\omega t} dt \\ &= \frac{1}{2\pi}\int_0^{2\pi} e^{iX_1 \sin(\tau) - iX_2 \cos(2\tau) - in\tau} d\tau. \end{aligned} \tag{3.12}$$

This integral form is close to a Bessel function but has no elementary solution thus we solve it numerically. The quasienergy matrix $\bar{Q}$ then has matrix elements

$$\bar{Q}_{m,m+n} = H_n - m\hbar\omega\delta_{n0} \tag{3.13}$$

We choose a cutoff for mode m, $|m| \leq m_c$, where m_c is a positive integer. This means we will have $N_m = 2m_c + 1$ diagonal blocks, where each block is a $N_S \times N_S$ matrix, H_n.

3.3 Floquet LLs in 2DEG

Next, similar to Dirac electrons, we consider the case of Schrödinger electrons under the application of two linearly polarized laser lights. The unperturbed Hamiltonian for 2DEG is

$$H = \frac{\pi_x^2}{2m^*} + \frac{\pi_y^2}{2m^*}, \tag{3.14}$$

where m^* is the effective mass of electron. By changing the Hamiltonian into a time-dependent form by applying two linearly polarized lights such that $\boldsymbol{\pi} \rightarrow \mathbf{p} - \mathbf{eA}(\mathbf{t})$. Therefore, Eq. (3.14) is written as

$$H(t) = \frac{1}{2m^*}[p_x + eA_x(t)]^2 + \frac{1}{2m^*}[p_y + eA_y(t)]^2, \tag{3.15}$$

where the electric field components for two spatially inhomogeneous linearly polarized laser lights are

$$\begin{aligned} \mathbf{E}_1 &= E\cos(\omega t)\mathbf{x}, \\ \mathbf{E}_2' &= E\cos(Kx)\sin(\omega t)\mathbf{y}. \end{aligned} \tag{3.16}$$

It is important to note that second electric field in Eq. (3.16) is different from similar field used for Dirac spectrum given in Eq. (3.2). This is due to the fact that Schrödinger Hamiltonian is quadratic rather than linear as in case of Dirac electrons. This is basic requirement for the Schrödinger electron spectrum to exhibit LLs. The field give in Eq. (3.16) lead to the following vector potential $\mathbf{A}(t)$

$$\mathbf{A}(t) = \langle -V_1\sin(\omega t), V_2\cos(\omega t), 0\rangle \tag{3.17}$$

where we have $V_1 = \frac{eE}{\omega}, V_2 = V_1\cos(Kx)$. Employing the Floquet theory similar to Dirac electrons, we obtain the effective Hamiltonian as

$$H_{\text{eff}} = H_0 - \frac{U}{m^*}\sin(Kx)p_y - \frac{U^2}{4m^*}V_1^2\cos(2Kx). \tag{3.18}$$

For Landau Level problem, we usually use the Landau gauge with vector potential like $A = (0, xB, 0), B = B\mathbf{z}$. In the long wavelength limit, Eq. (3.18) can be simplified to

$$H_{\text{eff}} = \frac{p_x^2}{2m^*} + \frac{1}{2m^*}[p_y + eBx]^2 - \frac{U^2}{4m^*}, \tag{3.19}$$

where $U = \frac{KV_1^2}{2m^*\omega}$, and the effective magnetic field $B = \frac{K^2V_1^2}{em^*\omega}$. Eq. (3.19) is a standard LL problem in the presence of an external perpendicular magnetic field. Therefore, by diagonalizing the effective Hamiltonian, the corresponding energy eigenvalues are obtained as

$$E_n = (n + \frac{1}{2})\hbar\omega_c - \frac{U^2}{4m^*}, \tag{3.20}$$

where $\omega_c = \frac{eB}{m^*}$. We can see from Eq. (3.20) that the effective magnetic field is directly proportional to the strength of the electric field (second order) and inversely proportional to the product of second order spatial period and third order of the frequency of the laser lights $\propto (E^2/(a^2\omega^3))$. This factor of the laser lights can be tuned to enhance the strength of the effective magnetic field in nonequilibrium systems.

3.4 Discussion and conclusion

Results can be explained with the help of existing experiments [67,69] and can provide an estimate for the strength of the effective magnetic field to observe LLs and QHE. Analytical structure of Eq. (3.7) and Eq. (3.20) is primarily responsible for the LLs spectrum in both the Dirac and Schrödinger systems, respectively. Although such results are valid for other 2D materials or Schrödinger systems, however, for simplicity, we will consider parameters realized for graphene or topological insulators [67, 69]. In these experiments [67, 69], the strength of the electric field used is 1×10^7 V/m to 1×10^8 V/m and the frequency of the light varies from 120 meV to 191 meV.

In case of Dirac electrons, we calculate the effective magnetic field strength using Eq. (3.7). For a fixed value of the spatial period of 120 nm and frequency of laser light $\hbar\omega = 191$ meV, the

strength of the effective magnetic field is ≈ 10 Tesla for electric field strength of 5×10^7 V/m [69]. Moreover, by reducing the spatial period to 12 nm, we obtain the effective magnetic field ≈ 98 Tesla for fixed frequency ($\hbar\omega$ = 191 meV) and electric field (5×10^7 V/m). This is due to the fact that effective magnetic field is directly proportional to electric field and inversely proportional to the spatial period of light according to Eq. (3.7). Similarly, keeping the spatial period constant and increasing the electric field strength, we can increase the strength of the effective magnetic field for larger frequencies only. However, for the frequency $\hbar\omega$ = 191 meV, we can not go beyond 5×10^7 V/m value of the electric field irrespective of the spatial period. This limitation is due to the factor "C" in Eq. (3.7). Further, using lower light frequency ($\hbar\omega$ = 120 meV) as realized in topological insulators experiments [67], the critical strength of the electric field is 2×10^7 V/m beyond which magnetic field will become negative. Additionally, for larger frequency of 220 meV, the maximum value of electric field 7×10^7 V/m can be used. It is also important and interesting to note that negative values of the effective magnetic field at larger strengths of light's electric field are fruitful. This is because positive or negative values of the effective magnetic field means (see Eq. (3.6)) that magnetic field is applied either from positive z-axis or negative z-axis. **This estimate of parameters is equally valid for frequency space expansion results (Fig. 1) obtained numerically and degenerate perturbation (Fig. 2) analysis.**

In case of Schrödinger electrons in conventional 2DEG systems, the effective magnetic field strength can be obtained using Eq. (3.20). For a fixed value of the spatial period of 100 nm and light frequency of $\hbar\omega$ = 191 meV, the strength of the effective magnetic field is 1 Tesla using electric field of 5×10^7 V/m. Further, by reducing the spatial period to 10 nm and keeping the electric field (5×10^7 V/m) and frequency of light ($\hbar\omega$ = 191 meV) fixed, we obtain the effective magnetic field ≈ 106 Tesla. This can be understood from Eq. (3.20). In contrast to Dirac case, by increasing the strength of electric field of light, we can increase the strength of the effective magnetic field values. For example, for fixed period of 100 nm and frequency ($\hbar\omega$ = 191 meV), the effective magnetic field is 17 Tesla for 2×10^8 V/m. Next, we see the impact of increasing or decreasing frequency and keeping period (100 nm) and electric field (5×10^7 V/m) fixed.

For decreasing frequency to 120 meV, we obtain larger effective magnetic field (4.3 Tesla) while increasing frequency leads to smaller effective magnetic field (0.7 Tesla at 220 meV light frequency). **This estimate of parameters is equally valid for frequency space expansion results (Fig. 1) obtained numerically and degenerate perturbation (Fig. 2) analysis.**

In conclusion, we have shown Floquet LLs and the QHE using two linearly polarized lights for graphene-like 2D and conventional 2DEG systems. While using these laser lights, we need at least one or both polarized lights to be spatially inhomogeneous. We have presented results using frequency space expansion method, degenerate Floquet perturbation theory, tight binding models and numerical model calculations. All the results are agreed well to show Floquet LLs in experimentally accessible parameters range. Also, it is interesting to note that we are flexible to use different values of the electric field strength, frequency or spatial period of the light to realize QHE and control the strength of the effective magnetic field. Therefore, we believe that Floquet LLs and QHE can be observed in the experiments for moderate strength of the spatially inhomogeneous lights **as shown in Figs. 1 and 2.** Moreover, we expect the potential to host new nano-electronics in nonequilibrium systems.

Chapter 4

Conclusion and Discussion

What makes gauge potential unique in creating/tuning/manipulating new topoglical systems Applications

Appendix A

Suitable Name

A.1 Kitaev Triangle and Peierls substitution

We start with a spinless or spin-polarized p-wave superconductor

$$\mathscr{H} = \sum_{\langle j,l \rangle} (-t c_j^\dagger c_l + \Delta e^{i\theta_{jl}} c_j c_l + h.c.) - \sum_j \mu c_j^\dagger c_j, \tag{A.1}$$

where t is the hopping amplitude, Δ is the amplitude of (2D) p-wave pairing, μ is the chemical potential, θ_{jl} is the polar angle of $\mathbf{r}_{jl} = \mathbf{r}_l - \mathbf{r}_j$, consistent with $\{c_l^\dagger, c_j^\dagger\} = 0$.

We will now include a gauge potential via a Peierls substitution as

$$\begin{aligned} c_j^\dagger &\to c_j^\dagger \exp\left(-\frac{ie}{\hbar}\int_0^{\mathbf{r}_j} \mathbf{A}\cdot d\mathbf{l}\right), \\ c_j^\dagger c_l &\to c_j^\dagger c_l \exp\left(\frac{ie}{\hbar}\int_{\mathbf{r}_j}^{\mathbf{r}_l} \mathbf{A}\cdot d\mathbf{l}\right) \\ &\to c_l^\dagger c_j e^{i\phi_{j,l}}. \\ \phi_{jl} &= \frac{e}{\hbar}\int_{\mathbf{r}_j}^{\mathbf{r}_l} \mathbf{A}\cdot d\mathbf{l} = -\phi_{lj} \end{aligned} \tag{A.2}$$

The modified Hamiltonian is then

$$\mathscr{H} = \sum_{\langle j,l \rangle} (-t e^{i\phi_{jl}} c_j^\dagger c_l + \Delta e^{i\theta_{jl}} c_j c_l + h.c.) - \sum_j \mu c_j^\dagger c_j, \tag{A.3}$$

The complex fermion operator can be written in the Majorana Fermion basis, a superposition of two Majorana fermions $c_j = \frac{1}{2}(a_j + i b_j)$. Due to the nature of Majorana fermions, $a_j^\dagger = a_j$, the creation operator is $c_j^\dagger = \frac{1}{2}(a_j - i b_j)$. It is quickly seen after substitution we arrive at

$$c_j^\dagger c_j = \frac{1}{2}(1 + i a_j b_j), \tag{A.4}$$

$$c_j^\dagger c_l = \frac{1}{4}(a_j a_l + b_j b_l + i a_j b_l - i b_j a_l), \tag{A.5}$$

$$c_j c_l = \frac{1}{4}(a_j a_l - b_j b_l + i a_j b_l + i b_j a_l). \tag{A.6}$$

The hopping term in MF basis are

$$-t(e^{i\phi_{jl}} c_j^\dagger c_l + e^{-i\phi_{jl}} c_l^\dagger c_j) = -\frac{it}{2}(\sin\phi_{jl}(a_j a_l + b_j b_l) + \cos\phi_{jl}(a_j b_l - b_j a_l)), \tag{A.7}$$

the order parameter terms are

$$\Delta(e^{i\theta_{jl}} c_j^\dagger c_l^\dagger + e^{-i\theta_{jl}} c_j c_l) = \frac{i\Delta}{2}(\sin\theta_{jl}(a_l a_j - b_l b_j) + \cos\theta_{jl}(a_l b_j + b_l a_j)). \tag{A.8}$$

Our Hamiltonian in MF basis is then

$$\begin{aligned}\mathscr{H} = -\frac{i}{2}\sum_{\langle j,l\rangle} [&(t\sin\phi_{jl} - \Delta\sin\theta_{jl}) a_j a_l + (t\sin\phi_{jl} + \Delta\sin\theta_{jl}) b_j b_l \\ &+ (t\cos\phi_{jl} - \Delta\cos\theta_{jl}) a_j b_l - (t\cos\phi_{jl} + \Delta\cos\theta_{jl}) b_j a_l] \\ -\frac{i\mu}{2}\sum_j a_j b_j\end{aligned} \tag{A.9}$$

For concreteness we consider a 1-D chain in the Kitaev limit $t = \Delta$, $\mu = 0$, and choose $phi_{jl} = 0$ (either zero or a perpendicular gauge potential). The Kitaev chain is resultant with $\mathscr{H} = -\sum_{j,j+1} i t b_j a_{j+1}$ and hosting MZM a_1 and b_N.

A.2 Conditions for MZM on equilateral triangular islands

We want to now use a gauge potential to tune our system into having zero modes located at the base corners of a triangular lattice. Consider first forming a minimal Kitaev triangle in the positive y-axis, with only 3-sites such that its base, with sites 1 and 2, are along the x-axis. While still considering the Kitaev limit in this minimal model, as previously stated, sites 1 and 2 form a Kitaev chain. In order for the MZM to persist in the presence of site 3, one can choose ϕ_{23} and ϕ_{31} so that all terms involving these Majorana operators cancel out. For example, consider the 2–3 bond, for which $\theta_{23} = 2\pi/3$, we require

$$\sin\phi_{jl} + \sin\frac{2\pi}{3} = \cos\phi_{jl} + \cos\frac{2\pi}{3} = 0 \tag{A.10}$$

which means $\phi_{23} = -\pi/3$. Similarly one can find $\phi_{31} = -\phi_{13} = -\pi/3$. The three Peierls phases can be realized by the following staggered vector potential

$$\mathbf{A} = [1 - 2\Theta(x)]\frac{2\pi}{3\sqrt{3}}\mathbf{y}. \tag{A.11}$$

Which is derived in the following subsection

A.2.1 Staggered vector potential

First, naively consider a constant vector potential field. For sites 1–2 we want the field to be perpendicular to their axis this tells usto start with $\mathbf{A} = A\mathbf{y}$. From Eq. A.2, set $e = \hbar = 1$ and the

line integral for ϕ_{13} becomes

$$\begin{aligned}
\phi_{13} &= \int_{\mathbf{r_1}}^{\mathbf{r_3}} \mathbf{A}\cdot d\mathbf{l} \\
&= A\int_{y_1}^{y_3} \mathbf{y}\cdot d\mathbf{l} \\
&= A\int_0^{\sqrt{3}a/2} dy \\
&= \frac{\sqrt{3}Aa}{2} \\
&= \pi/3.
\end{aligned}$$

We find that we need

$$A = \frac{2\pi}{3\sqrt{3}a}. \tag{A.12}$$

Now let us check if this allows for $\phi_{23} = -\pi/3$.

$$\begin{aligned}
\phi_{23} &= \int_{\mathbf{r_2}}^{\mathbf{r_3}} \mathbf{A}\cdot d\mathbf{l} \\
&= A\int_{y_2}^{y_3} \mathbf{y}\cdot d\mathbf{l} \\
&= A\int_0^{\sqrt{3}a/2} dy \\
&= \frac{\sqrt{3}Aa}{2} \\
&= \frac{\sqrt{3}a}{2}\frac{2\pi}{3\sqrt{3}a} \\
&= \pi/3 \neq -\pi/3.
\end{aligned}$$

Here we see that a constant vector potential does not meet the condition for MZM, it's off by a sign factor. This is remedied by using the Heaviside function instead from equation A.11

$$\mathbf{A} = [1 - 2\Theta(x)]\frac{2\pi}{3\sqrt{3}}\mathbf{y}.$$

A.2.2 Linear vector potential

While the simplest vector potential one can use in the minimal Kitaev triangle is a staggered potential it remains to be seen if other odd functions also work. Again, we want the Peierls phase for sites 1–2 to have no contribution, let $\mathbf{A} = Ax\mathbf{y}$. Simlarly, for sites 1–3 we have

$$\begin{aligned}
\phi_{13} &= \int_{\mathbf{r_1}}^{\mathbf{r_3}} \mathbf{A}\cdot d\mathbf{l} \\
&= \int_{y_1}^{y_3} Ax dy \\
&= \int_{x_1}^{x_3} Ax\frac{dy}{dx}dx \\
&= \sqrt{3}A\int_{-a/2}^{0} x dx \\
&= -\frac{\sqrt{3}Aa^2}{8} \\
&= \pi/3.
\end{aligned}$$

The magnitude is then

$$A = -\frac{8\pi}{3\sqrt{3}a^2}. \tag{A.13}$$

Check if $\phi_{23} = -\pi/3$:

$$\begin{aligned}
\phi_{23} &= \int_{x_2}^{x_3} Ax \frac{dy}{dx} dx \\
&= -\sqrt{3}A \int_{a/2}^{0} x dx \\
&= A\left(\frac{\sqrt{3}a^2}{8}\right) \\
&= -\frac{8\pi}{3\sqrt{3}a^2}\left(\frac{\sqrt{3}a^2}{8}\right) \\
&= -\pi/3.
\end{aligned}$$

We have shown a linear vector potential (symmetric/centered about the y-axis) can host MZM on a minimal Kitaev triangle's base corners. In general, this should be true for any odd function used

Triangle Length and Vector Potential Strength

For a staggered vector potential such as a Heaviside or Tanh function we do not need to adjust the vector potential strength relative to its size. When considering larger Kitaev triangles we need to adjust the vector potential strength for linear and higher order vector potentials. Start with the botton left corner point, x_j, and look at its nearest neighbor along $\theta = \pi/3$, we denote this point with position x_l. If we look back at the line integral of a linear function we have the general form of

$$\begin{aligned}
\phi_{jl} &= A \int_{x_j}^{x_l} \frac{dy}{dx} x dx \\
&= \frac{\sqrt{3}A}{2}(x_l^2 - x_j^2) = \pi/3.
\end{aligned}$$

We can rearrange to get

$$A = \frac{2\pi}{3\sqrt{3}} \frac{1}{x_l^2 - x_j^2}. \tag{A.14}$$

A more simplified solution follows. For the outer length of a triangle we use `nr` to denote the number of rows the triangle has, it is one of the first few defined variables in a given script. The positions x_j and x_l have simple linear relations in regards to `nr`. Due to the equilateral nature of our triangle and centering about the y-axis

$$x_l = \frac{-a}{2}(\texttt{nr} - 1). \tag{A.15}$$

It's easy to see that $x_l = x_j + a/2$ which gives

$$x_l = \frac{-a}{2}(\texttt{nr} - 2). \tag{A.16}$$

Now, the difference of the squares is

$$x_l^2 - x_j^2 = \frac{-a^2}{4}(2\texttt{nr} - 3). \tag{A.17}$$

Plugging back into our expression we find

$$-\frac{8\pi}{3\sqrt{3}a^2(2\texttt{nr} - 3)}. \tag{A.18}$$

This is expression is easy to implement in code.

A.3 Tight-binding model 2DEG

We start with a nearest-neighbor single-orbital tight-binding Hamiltonian on a square lattice

$$\mathscr{H} = \sum_{j,l} -h(c^{\dagger}_{j,l}c_{j+1,l} + c^{\dagger}_{j,l}c_{j,l+1} + h.c.) \tag{A.19}$$

The incident laser beam as a vector potential is as follows

$$\mathbf{A}(\mathbf{r}, t) = \frac{E}{\omega}\langle -\sin\omega t, \cos(Kx)\cos\omega t\rangle. \tag{A.20}$$

Using the following approximation for smoothly varying vector potential fields

$$\int_{\mathbf{r}_a}^{\mathbf{r}_b} \mathbf{A}(\mathbf{r}, t)\cdot d\mathbf{l} \approx \mathbf{A}\Big(\frac{\mathbf{r}_b + \mathbf{r}_b}{2}, t\Big)\cdot(\mathbf{r}_b - \mathbf{r}_a) \tag{A.21}$$

and using Peierls substitution the Hamiltonian becomes

$$\mathscr{H}(t) = -\sum_{j,l}(h_{j,j+1}(t)c^{\dagger}_{j,l}c_{j+1,l} + h_{l,l+1}(t)c^{\dagger}_{j,l}c_{j,l+1} + h.c.), \tag{A.22}$$

where

$$\begin{aligned} h_{j,j+1}(t) &\approx h\exp\left(i\frac{eEa}{\hbar\omega}\frac{x_j - x_{j+1}}{a}\sin\omega t\right) \\ &= h\exp\big(i\phi_0\sin\omega t\big) \end{aligned} \tag{A.23}$$

$$\begin{aligned} h_{l,l+1}(t) &\approx h\exp\left(i\frac{eEa}{\hbar\omega}\frac{y_{l+1} - y_l}{a}\cos\big(Kx_j\big)\cos\omega t\right) \\ &= h\exp\big(i\phi_0\cos\big(Kx_j\big)\cos\omega t\big). \end{aligned} \tag{A.24}$$

The incident laser beam allows for translation symmetry along the y-axis, so we can reduce the dimension of the Hamiltonian with the following Fourier transform

$$c^{\dagger}_{j,l} = \frac{1}{\sqrt{N_y}}\sum_k c^{\dagger}_{j,k}e^{ik\mathbf{y}\cdot\mathbf{r}_l} = \frac{1}{\sqrt{N_y}}\sum_k c^{\dagger}_{j,k}e^{ikla}. \tag{A.25}$$

The Hamiltonian then becomes

$$\mathscr{H}(t) = \sum_{j,k} (h_{l,l+1}(t)e^{-ika} + h^*_{l,l+1}(t)e^{ika}) c^\dagger_{j,k} c_{j,k} + (h_{j,j+1}(t) c^\dagger_{j,k} c_{j+1,k} + h.c.) \tag{A.26}$$

$$= \sum_{j,k} 2h \cos\big(\phi_0 \cos\big(Kx_j\big) \cos\omega t - ka\big) c^\dagger_{j,k} c_{j,k} + (he^{i\phi_0 \sin\omega t} c^\dagger_{j,k} c_{j+1,k} + h.c.). \tag{A.27}$$

Making use of Floquet theory we can make the Hamiltonian time-independent with the following time Fourier transform

$$\mathscr{H}_{ab,n}(k) = \frac{1}{T}\int_0^T \mathscr{H}_{ab}(k,t) e^{-in\omega t} dt \tag{A.28}$$

$$= \frac{1}{2\pi}\int_0^{2\pi} \mathscr{H}_{ab}(k,t) e^{-in\tau} d\tau \tag{A.29}$$

where a, b represent the matrix index of the previous Hamiltonian and n is the n-th order mode of light. We will make use of the following Hansen-Bessel integral formulas

$$J_n(z) = \frac{1}{2\pi}\int_0^{2\pi} e^{in\tau - z\sin\tau} d\tau = \frac{1}{2\pi}\int_0^{2\pi} e^{in\tau - in\pi/2 + z\cos\tau} d\tau, \tag{A.30}$$

note that the integral bound can be the same due to the integrand being periodic from $[0, 2\pi]$. Recall, Bessel function identities for $n \in \mathbb{Z}$

$$J_n(-z) = (-1)^n J_n(z) \tag{A.31}$$

$$J_{-n}(z) = (-1)^n J_n(z) \tag{A.32}$$

The terms for given k become the following time Fourier transforms

$$\begin{aligned}
\mathscr{H}_{j,j,n}(k) &= -\frac{h}{2\pi}\int_0^{2\pi}\left(e^{i\phi_0\cos(Kx_j)\cos\tau - ika - in\tau} + e^{-i\phi_0\cos(Kx_j)\cos\tau + ika - in\tau}\right)d\tau \\
&= -h\left(\frac{e^{-ika}}{2\pi}\int_0^{2\pi} e^{iz\cos\tau - in\tau}\,d\tau + \frac{e^{ika}}{2\pi}\int_0^{2\pi} e^{-iz\cos\tau - in\tau}\,d\tau\right) \\
&= -h\left(\frac{e^{-ika-in\pi/2}}{2\pi}\int_0^{2\pi} e^{iz\cos\tau - in\tau + in\pi/2}\,d\tau + \frac{e^{ika-in\pi/2}}{2\pi}\int_0^{2\pi} e^{-iz\cos\tau - in\tau + in\pi/2}\,d\tau\right) \\
&= -he^{-in\pi/2}\left(J_{-n}(z)e^{-ika} + J_{-n}(-z)e^{ika}\right) \\
&= -hJ_n(z)e^{-in\pi/2}(e^{ika} + e^{-ika+in\pi}) \\
&= -hJ_n(z)(e^{i(ka-n\pi/2)} + e^{-i(ka-n\pi/2)}) \\
&= -2hJ_n(\phi_0\cos(Kx_j))\cos(ka - n\pi/2)
\end{aligned} \tag{A.33}$$

and

$$\begin{aligned}
\mathscr{H}_{j,j+1,n} &= -\frac{h}{2\pi}\int_0^{2\pi} e^{i\phi_0\sin\tau - in\tau}\,d\tau \\
&= -hJ_{-n}(-\phi_0) \\
&= -hJ_n(\phi_0)
\end{aligned} \tag{A.34}$$

$$\begin{aligned}
\mathscr{H}_{j+1,j,n} &= -\frac{h}{2\pi}\int_0^{2\pi} e^{-i\phi_0\sin\tau - in\tau}\,d\tau \\
&= -hJ_{-n}(\phi_0) \\
&= -h(-1)^n J_n(\phi_0)
\end{aligned} \tag{A.35}$$

This completes finding all the matrix terms for the quasienergy matrix $\bar{Q}$ for a 2DEG tight binding model with incident inhomogeneous laser light.

A.4 Tight-binding model Dirac

We start with a nearest-neighbor single-orbital tight-binding Hamiltonian

$$\mathscr{H} = -\sum_{jl\alpha, j'l'\beta} hc^{\dagger}_{jl\alpha} c_{j'l'\beta} + h.c. \tag{A.36}$$

The incident laser beam in vector potential forms looks like

$$\mathbf{A}(\mathbf{r}, t) = \frac{E}{\omega}\langle -\sin\omega t, \frac{1}{2}\sin(Kx)\cos 2\omega t\rangle. \tag{A.37}$$

Using the following approximation for smoothly varying vector potential fields

$$\int_{\mathbf{r}^{\alpha}_{j,l}}^{\mathbf{r}^{\beta}_{j',l'}} \mathbf{A}(\mathbf{r}, t)\cdot d\mathbf{l} \approx \mathbf{A}\left(\frac{\mathbf{r}^{\beta}_{j',l'} + \mathbf{r}^{\alpha}_{j,l}}{2}, t\right)\cdot\left(\mathbf{r}^{\beta}_{j',l'} - \mathbf{r}^{\alpha}_{j,l}\right) \tag{A.38}$$

where

$$\mathbf{a}_1 = \sqrt{3}a\mathbf{x} \tag{A.39}$$

$$\mathbf{a}_2 = 3a\mathbf{y} \tag{A.40}$$

$$\mathbf{r}^{A_1}_{jl} = j\mathbf{a}_1 + l\mathbf{a}_2 \tag{A.41}$$

$$\mathbf{r}^{B_1}_{jl} = (j+\tfrac{1}{2})\mathbf{a}_1 + (l+\tfrac{1}{6})\mathbf{a}_2 \tag{A.42}$$

$$\mathbf{r}^{A_2}_{jl} = (j+\tfrac{1}{2})\mathbf{a}_1 + (l+\tfrac{1}{2})\mathbf{a}_2 \tag{A.43}$$

$$\mathbf{r}^{B_2}_{jl} = (j+1)\mathbf{a}_1 + (l+\tfrac{2}{3})\mathbf{a}_2. \tag{A.44}$$

Applying a Peierls substitution the Hamiltonian becomes

$$\begin{aligned}\mathscr{H}(t) = -\sum_{jl} & h_{jlA_1}^{jlB_1}(t)c_{jlA_1}^{\dagger}c_{jlB_1} + h_{jlB_1}^{jlA_2}(t)c_{jlB_1}^{\dagger}c_{jlA_2} + h_{jlA_2}^{jlB_2}(t)c_{jlA_2}^{\dagger}c_{jlB_2} \\ & + h_{jlB_1}^{j+1,lA_1}(t)c_{jlB_1}^{\dagger}c_{j+1,lA_1} + h_{jlB_2}^{j+1,l,A_2}c_{jlB_2}^{\dagger}c_{j+1,lA_2}(t) \\ & + h_{jlB_2}^{j+1,l+1,A_1}(t)c_{jlB_2}^{\dagger}c_{j+1,l+1,A_1} + h.c.\end{aligned} \tag{A.45}$$

where in general

$$h_{jl\alpha}^{j'l'\beta}(t) \approx h\exp\left[i\phi_0\left(-\frac{x_{j'l'}^{\beta}-x_{jl}^{\alpha}}{a}\sin\omega t + \frac{y_{j'l'}^{\beta}-y_{jl}^{\alpha}}{2a}\sin\left(K\frac{x_{j'l'}^{\beta}+x_{jl}^{\alpha}}{2}\right)\cos 2\omega t\right)\right]. \tag{A.46}$$

More explicitly for each term

$$h_{jlA_1}^{jlB_1}(t) \approx h\exp\left[i\phi_0\left(-\frac{\sqrt{3}}{2}\sin\omega t + \frac{1}{4}\sin\left(\sqrt{3}Ka(j+\tfrac{1}{4})\right)\cos 2\omega t\right)\right] \tag{A.47}$$

$$h_{jlB_1}^{jlA_2}(t) \approx h\exp\left[i\phi_0\left(\frac{1}{2}\sin\left(\sqrt{3}Ka(j+\tfrac{1}{2})\right)\cos 2\omega t\right)\right] \tag{A.48}$$

$$h_{jlA_2}^{jlB_2}(t) \approx h\exp\left[i\phi_0\left(-\frac{\sqrt{3}}{2}\sin\omega t + \frac{1}{4}\sin\left(\sqrt{3}Ka(j+\tfrac{3}{4})\right)\cos 2\omega t\right)\right] \tag{A.49}$$

$$h_{jlB_1}^{j+1,lA_1}(t) \approx h\exp\left[i\phi_0\left(-\frac{\sqrt{3}}{2}\sin\omega t - \frac{1}{4}\sin\left(\sqrt{3}Ka(j+\tfrac{3}{4})\right)\cos 2\omega t\right)\right] \tag{A.50}$$

$$h_{jlB_2}^{j+1,lA_2}(t) \approx h\exp\left[i\phi_0\left(-\frac{\sqrt{3}}{2}\sin\omega t - \frac{1}{4}\sin\left(\sqrt{3}Ka(j+\tfrac{5}{4})\right)\cos 2\omega t\right)\right] \tag{A.51}$$

$$h_{jlB_2}^{j+1,l+1,A_1}(t) \approx h\exp\left[i\phi_0\left(\frac{1}{2}\sin\left(\sqrt{3}Ka(j+1)\right)\cos 2\omega t\right)\right] \tag{A.52}$$

The incident laser beam allows for translation symmetry along the y-axis, so we can reduce the dimension of the Hamiltonian with the following Fourier transform

$$c^{\dagger}_{jl\alpha} = \frac{1}{N_y}\sum_k c^{\dagger}_{jk\alpha} e^{ik\mathbf{y}\cdot\mathbf{R_l}} = \frac{1}{N_y}\sum_k c^{\dagger}_{jk\alpha} e^{ik(3la)} \tag{A.53}$$

The Hamiltonian then becomes

$$\begin{aligned}\mathscr{H}(t) = -\sum_{jk} & h^{jlB_1}_{jlA_1}(t)c^{\dagger}_{jkA_1}c_{jkB_1} + h^{jlA_2}_{jlB_1}(t)c^{\dagger}_{jkB_1}c_{jkA_2} + h^{jlB_2}_{jlA_2}(t)c^{\dagger}_{jkA_2}c_{jkB_2} \\ & + h^{j+1,lA_1}_{jlB_1}(t)c^{\dagger}_{jkB_1}c_{j+1,kA_1} + h^{j+1,l,A_2}_{jlB_2}c^{\dagger}_{jkB_2}c_{j+1,kA_2}(t) \\ & + h^{j+1,l+1,A_1}_{jlB_2}(t)e^{-i3ka}c^{\dagger}_{jkB_2}c_{j+1,kA_1} + h.c.\end{aligned} \tag{A.54}$$

Making use of Floquet theory we can make the Hamiltonian time-independent with the following time domain Fourier transform

$$\mathscr{H}_{ab,n}(k) = \frac{1}{2\pi}\int_0^{2\pi} \mathscr{H}_{ab}(k,t)e^{-in\tau}d\tau \tag{A.55}$$

where a, b represent the amtrix indes of the previous Hamiltonian and n is the n-th order mode of light. Each term has the general following form

$$\mathscr{H}_{ab,n}(k) = \frac{1}{2\pi}\int_0^{2\pi} e^{iZ_1\sin\tau + iZ_2\cos 2\tau - in\tau}d\tau \tag{A.56}$$

which looks a lot like the Hansen-Bessel integral function. However, because of the linear combination of $\sin\tau$ and $\cos 2\tau$, there is no elementary solution to the integral as currently defined. I think if it was a linear combination of $\sin\tau$ and $\cos\tau$ we could use an addition of sines identity and maybe get a Hansen-Bessel integral. A moot point for this project since we need the $\cos 2\tau$ term to match the continuum models expectation of Landau levels. We thus solve the integral numerically for each given n. After the time domain Fourier transform the Hamiltonian can be

reduced to the following matrix form

$$\mathscr{H} = -\sum_{jk}\left[\Psi^{\dagger}_{jk}\mathscr{H}_{jj}\Psi_{jk} + \Psi^{\dagger}_{jk}\mathscr{H}'_{j,j+1}(k)\Psi_{j+1,k} + h.c.\right] \tag{A.57}$$

$$\mathscr{H}_{jj} = \begin{bmatrix} 0 & h^{jlB_2}_{jlA_1} & 0 & 0 \\ 0 & 0 & h^{jlA_2}_{jlB_1} & 0 \\ 0 & 0 & 0 & h^{jlB_2}_{jlA_2} \\ 0 & 0 & 0 & 0 \end{bmatrix}$$

$$\mathscr{H}'_{j,j+1}(k) = \begin{bmatrix} 0 & 0 & 0 & 0 \\ h^{j+1,lA_1}_{jlB_1} & 0 & 0 & 0 \\ 0 & 0 & 0 & 0 \\ e^{-i3ka}h^{j+1,l+1,A_1}_{jlB_2} & 0 & h^{j+1,lA_2}_{jlB_2} & 0 \end{bmatrix}$$

with $\Psi_{jk} = [c_{jkA_1}, c_{jkB_1}, c_{jkA_2}, c_{jkB_2}]^T$.

A.5 Quantum harmonic oscillator

We will quickly derive this energy solution and derive ladder operators. Rewrite the quantum harmonic oscillator as (and dropping the operator hat)

$$H = \frac{1}{2m}\left(p_x^2 + m^2\omega^2 x^2\right),$$

then complete the square by adding "zero"

$$
\begin{aligned}
H &= \frac{1}{2m}\left([m\omega x - ip_x][m\omega x + ip_x] - im\omega[xp_x - p_x x]\right) \\
&= \frac{1}{2m}\left([m\omega x - ip_x][m\omega + ip_x] + m\hbar\omega\right) \\
&= \frac{1}{2m}\left(\tilde{a}^\dagger \tilde{a} + m\hbar\omega\right) \\
&= \hbar\omega\left(\frac{\tilde{a}^\dagger \tilde{a}}{2m\hbar\omega} + \frac{1}{2}\right) \\
&= \hbar\omega\left(a^\dagger a + \frac{1}{2}\right), \qquad \text{(A.58)}
\end{aligned}
$$

where $a = \frac{1}{\sqrt{2}}\left(\sqrt{\frac{m\omega}{\hbar}}x + i\frac{p_x}{\sqrt{m\hbar\omega}}\right)$. We have simplified the Hamiltonian into new creation and annihilation operators, called ladder operators, which we will now show how they work. Also note $[a, a^\dagger] = 1$. Let looks at how the operator commutes with the Hamiltonian

$$
\begin{aligned}
[H, a] &= Ha - aH = \hbar\omega\left(a^\dagger aa + \frac{a}{2} - aa^\dagger a - \frac{a}{2})\right) \\
&= \hbar\omega(a^\dagger a - (1 + a^\dagger a))a \\
&= -\hbar\omega a, \quad \text{and} \qquad \text{(A.59)} \\
[H, a^\dagger] &= Ha^\dagger - a^\dagger H = \hbar\omega\left(a^\dagger aa^\dagger + \frac{a^\dagger}{2} - a^\dagger a^\dagger a - \frac{a^\dagger}{2}\right) \\
&= \hbar\omega a^\dagger(aa^\dagger - a^\dagger a) \\
&= \hbar\omega a^\dagger. \qquad \text{(A.60)}
\end{aligned}
$$

SOME TRANSITION TO ACTING Ha on Psi.

$$
\begin{aligned}
H|\psi_n\rangle &= E_n|\psi_n\rangle. \\
Ha^\dagger|\psi_n\rangle &= (a^\dagger H + \hbar\omega a^\dagger)|\psi_n\rangle \\
Ha^\dagger|\psi_n\rangle &= (E_n + \hbar\omega)a^\dagger|\psi_n\rangle. \\
Ha|\psi_n\rangle &= (E_n - \hbar\omega)a|\psi_n\rangle.
\end{aligned}
\tag{A.61}
$$

Being careful notice

$$
\begin{aligned}
H|\psi_0\rangle &= E_0|\psi_0\rangle \\
Ha|\psi_0\rangle &= (E_0 - \hbar\omega)a|\psi_0\rangle,
\end{aligned}
\tag{A.62}
$$

however, E_0 is the minimum so $E_0 - \hbar\omega$ cannot exist and thus

$$
a|\psi_0\rangle = 0 \tag{A.63}
$$

Again we look at the ground state energy

$$
\begin{aligned}
\langle\psi_0|H|\psi_0\rangle &= \langle\psi_0|\hbar\omega(a^\dagger a + 1/2)|\psi_0\rangle \\
E_0 &= \hbar\omega\langle\psi_0|a^\dagger a|\psi_0\rangle + \frac{\hbar\omega}{2}\langle\psi_0|\psi_0\rangle \\
E_0 &= \frac{\hbar\omega}{2}.
\end{aligned}
\tag{A.64}
$$

Then for the given eigenstates

$$a^\dagger|\psi_0\rangle, \quad a^\dagger a^\dagger|\psi_0\rangle, \quad a^\dagger a^\dagger a^\dagger|\psi_0\rangle, \quad \ldots$$

with eigenvalues

$$\tfrac{3}{2}\hbar\omega, \quad \tfrac{5}{2}\hbar\omega, \quad \tfrac{7}{2}\hbar\omega, \quad \ldots$$

Which we can generalize to

$$|\psi_n\rangle \propto (a^\dagger)^n|\psi_0\rangle,$$

with the eigenenergy

$$E_n = \hbar\omega\left(n+\tfrac{1}{2}\right).$$

With our goal complete we continue on to determine how the ladder operators evolve the state.

We can now renormalize our proportional expression

$$|\psi_{n+1}\rangle = ca^\dagger|\psi_n\rangle$$

$$\begin{aligned}
1 = \langle\psi_{n+1}|\psi_{n+1}\rangle &= |c|^2(\langle\psi_n|a^\dagger)(a^\dagger|\psi_n\rangle) \\
&= |c|^2\langle\psi_n|aa^\dagger|\psi_n\rangle \\
&= |c|^2\langle\psi_n|\frac{H}{\hbar\omega}+\frac{1}{2}|\psi_n\rangle \\
&= |c|^2\left(\frac{E_n}{\hbar\omega}+\frac{1}{2}\right) \\
&= |c|^2(n+1)
\end{aligned}$$

$$|c| = \frac{1}{\sqrt{n+1}}$$

which give the following relation

$$|\psi_{n+1}\rangle = \frac{a^\dagger}{\sqrt{n+1}}|\psi_n\rangle. \tag{A.65}$$

Similarly we find

$$|\psi_{n-1}\rangle = \frac{a^\dagger}{\sqrt{n}}|\psi_n\rangle. \tag{A.66}$$

Thus $a^\dagger a|\psi_n\rangle = n|\psi_n\rangle$. The energy of the system is definitively

$$E_n = \hbar\omega\left(n + \frac{1}{2}\right) \tag{A.67}$$

A.6 Dirac equation in the presence of a magnetic field

We now focus on how the presence of a magnetic field affects the Dirac equation. The Dirac Hamiltonian with vector potential

$$\mathscr{H} = v_f \boldsymbol{\sigma} \cdot (\hat{p} - q\hat{A}) \tag{A.68}$$

Using the previous definition, $\mathbf{A} = Bx\mathbf{y}$, the Hamiltonian becomes

$$\mathscr{H} = v_f \sigma_x \hat{p}_x + v_f \sigma_y (\hat{p}_y - qB\hat{x}) \tag{A.69}$$

Like Schrodinger's equation we use the same ansatz wavefunction and arrive at

$$\mathscr{H} = v_f \sigma_x \hat{p}_x - v_f \sigma_y (qB\hat{x} - \hbar k_y)$$

$$\mathscr{H} = v_f \sigma_x \hat{p}_x - v_f \sigma_y qB\hat{x}, \tag{A.70}$$

where we recognize the x term is just shifted by a constant like earlier. In matrix form the Hamiltonian looks like

$$\mathscr{H} = i v_f qB \begin{bmatrix} 0 & \hat{x} - i\dfrac{\hat{p}_x}{qB} \\ \hat{x} + i\dfrac{\hat{p}_x}{qB} & 0 \end{bmatrix}$$

$$\mathscr{H} = i v_f \sqrt{2m\hbar\omega} \begin{bmatrix} 0 & a^\dagger \\ a & 0 \end{bmatrix}$$

The form of the Hamiltonian can be quickly solved by squaring then acting on a wavefunction

$$|\mathscr{H}|^2 = 2m\hbar\omega v_f^2 \begin{bmatrix} a^\dagger a & 0 \\ 0 & aa^\dagger \end{bmatrix}$$

We focus on the first element of the matrix

$$\begin{aligned} \langle\psi_n||\mathscr{H}_{11}|^2|\psi_n\rangle &= \langle\psi_n|E_n^2|\psi_n\rangle \\ &= 2m\hbar\omega v_f^2 \langle\psi_n|a^\dagger a|\psi_n\rangle \\ &= 2m\hbar\omega v_f^2 \langle\psi_n|n|\psi_n\rangle \\ E_n^2 &= 2m\hbar\omega n v_f^2 \\ E_n &= \pm v_f \sqrt{2m\hbar\omega n} \end{aligned} \tag{A.71}$$

Bibliography

[1] D. A. Ivanov. Non-Abelian Statistics of Half-Quantum Vortices in p -Wave Superconductors. *Phys. Rev. Lett.*, 86(2):268–271, January 2001.

[2] A. Yu. Kitaev. Fault-tolerant quantum computation by anyons. *Annals of Physics*, 303(1):2–30, January 2003.

[3] Chetan Nayak, Steven H. Simon, Ady Stern, Michael Freedman, and Sankar Das Sarma. Non-Abelian anyons and topological quantum computation. *Rev. Mod. Phys.*, 80(3):1083–1159, September 2008.

[4] Jason Alicea, Yuval Oreg, Gil Refael, Felix von Oppen, and Matthew P. A. Fisher. Non-Abelian statistics and topological quantum information processing in 1D wire networks. *Nature Phys*, 7(5):412–417, May 2011.

[5] David Aasen, Michael Hell, Ryan V. Mishmash, Andrew Higginbotham, Jeroen Danon, Martin Leijnse, Thomas S. Jespersen, Joshua A. Folk, Charles M. Marcus, Karsten Flensberg, and Jason Alicea. Milestones Toward Majorana-Based Quantum Computing. *Phys. Rev. X*, 6(3):031016, August 2016.

[6] N. Read and Dmitry Green. Paired states of fermions in two dimensions with breaking of parity and time-reversal symmetries and the fractional quantum Hall effect. *Phys. Rev. B*, 61(15):10267–10297, April 2000.

[7] A. Yu Kitaev. Unpaired Majorana fermions in quantum wires. *Phys.-Usp.*, 44(10S):131, October 2001.

[8] Jean-Pascal Brison. P-Wave Superconductivity and d-Vector Representation. In Hervé Bulou, Loïc Joly, Jean-Michel Mariot, and Fabrice Scheurer, editors, *Magnetism and Accelerator-Based Light Sources*, Springer Proceedings in Physics, pages 165–204, Cham, 2021. Springer International Publishing.

[9] V. Mourik, K. Zuo, S. M. Frolov, S. R. Plissard, E. P. A. M. Bakkers, and L. P. Kouwenhoven. Signatures of Majorana Fermions in Hybrid Superconductor-Semiconductor Nanowire Devices. *Science*, 336(6084):1003–1007, May 2012.

[10] Leonid P. Rokhinson, Xinyu Liu, and Jacek K. Furdyna. The fractional a.c. Josephson effect in a semiconductor–superconductor nanowire as a signature of Majorana particles. *Nature Phys*, 8(11):795–799, November 2012.

[11] M. T. Deng, C. L. Yu, G. Y. Huang, M. Larsson, P. Caroff, and H. Q. Xu. Anomalous Zero-Bias Conductance Peak in a Nb–InSb Nanowire–Nb Hybrid Device. *Nano Lett.*, 12(12):6414–6419, December 2012.

[12] T.-P. Choy, J. M. Edge, A. R. Akhmerov, and C. W. J. Beenakker. Majorana fermions emerging from magnetic nanoparticles on a superconductor without spin-orbit coupling. *Phys. Rev. B*, 84(19):195442, November 2011.

[13] Bernd Braunecker and Pascal Simon. Interplay between Classical Magnetic Moments and Superconductivity in Quantum One-Dimensional Conductors: Toward a Self-Sustained Topological Majorana Phase. *Phys. Rev. Lett.*, 111(14):147202, October 2013.

[14] Jelena Klinovaja, Peter Stano, Ali Yazdani, and Daniel Loss. Topological Superconductivity and Majorana Fermions in RKKY Systems. *Phys. Rev. Lett.*, 111(18):186805, November 2013.

[15] S. Nadj-Perge, I. K. Drozdov, B. A. Bernevig, and Ali Yazdani. Proposal for realizing Majorana fermions in chains of magnetic atoms on a superconductor. *Phys. Rev. B*, 88(2):020407, July 2013.

[16] Stevan Nadj-Perge, Ilya K. Drozdov, Jian Li, Hua Chen, Sangjun Jeon, Jungpil Seo, Allan H. MacDonald, B. Andrei Bernevig, and Ali Yazdani. Observation of Majorana fermions in ferromagnetic atomic chains on a superconductor. *Science*, 346(6209):602–607, October 2014.

[17] Lucas Schneider, Philip Beck, Jannis Neuhaus-Steinmetz, Levente Rózsa, Thore Posske, Jens Wiebe, and Roland Wiesendanger. Precursors of Majorana modes and their length-dependent energy oscillations probed at both ends of atomic Shiba chains. *Nat. Nanotechnol.*, 17(4):384–389, April 2022.

[18] Liang Fu and C. L. Kane. Superconducting proximity effect and Majorana fermions at the surface of a topological insulator. *Phys. Rev. Lett.*, 100(9):096407, March 2008.

[19] Pavan Hosur, Pouyan Ghaemi, Roger S. K. Mong, and Ashvin Vishwanath. Majorana Modes at the Ends of Superconductor Vortices in Doped Topological Insulators. *Phys. Rev. Lett.*, 107(9):097001, August 2011.

[20] Andrew C. Potter and Patrick A. Lee. Engineering a $p+\mathit{ip}$ superconductor: Comparison of topological insulator and Rashba spin-orbit-coupled materials. *Phys. Rev. B*, 83(18):184520, May 2011.

[21] M. Veldhorst, M. Snelder, M. Hoek, C. G. Molenaar, D. P. Leusink, A. A. Golubov, H. Hilgenkamp, and A. Brinkman. Magnetotransport and induced superconductivity in Bi based three-dimensional topological insulators. *physica status solidi (RRL) – Rapid Research Letters*, 7(1-2):26–38, 2013.

[22] Chui-Zhen Chen, Ying-Ming Xie, Jie Liu, Patrick A. Lee, and K. T. Law. Quasi-one-dimensional quantum anomalous Hall systems as new platforms for scalable topological quantum computation. *Phys. Rev. B*, 97(10):104504, March 2018.

[23] Yongxin Zeng, Chao Lei, Gaurav Chaudhary, and Allan H. MacDonald. Quantum anomalous Hall Majorana platform. *Phys. Rev. B*, 97(8):081102, February 2018.

[24] Ying-Ming Xie, Xue-Jian Gao, Tai-Kai Ng, and K. T. Law. Creating Localized Majorana Zero Modes in Quantum Anomalous Hall Insulator/Superconductor Heterostructures with a Scissor, June 2021.

[25] Yuval Oreg, Gil Refael, and Felix von Oppen. Helical Liquids and Majorana Bound States in Quantum Wires. *Phys. Rev. Lett.*, 105(17):177002, October 2010.

[26] Jay D. Sau, Roman M. Lutchyn, Sumanta Tewari, and S. Das Sarma. Generic New Platform for Topological Quantum Computation Using Semiconductor Heterostructures. *Phys. Rev. Lett.*, 104(4):040502, January 2010.

[27] Roman M. Lutchyn, Tudor D. Stanescu, and S. Das Sarma. Search for Majorana Fermions in Multiband Semiconducting Nanowires. *Phys. Rev. Lett.*, 106(12):127001, March 2011.

[28] Andrew C. Potter and Patrick A. Lee. Topological superconductivity and Majorana fermions in metallic surface states. *Phys. Rev. B*, 85(9):094516, March 2012.

[29] Jian Li, Titus Neupert, Zhijun Wang, A. H. MacDonald, A. Yazdani, and B. Andrei Bernevig. Two-dimensional chiral topological superconductivity in Shiba lattices. *Nat Commun*, 7(1):12297, July 2016.

[30] Chao Lei, Hua Chen, and Allan H. MacDonald. Ultrathin Films of Superconducting Metals as a Platform for Topological Superconductivity. *Phys. Rev. Lett.*, 121(22):227701, November 2018.

[31] Annica M. Black-Schaffer and Jacob Linder. Majorana fermions in spin-orbit-coupled ferromagnetic Josephson junctions. *Phys. Rev. B*, 84(18):180509, November 2011.

[32] Falko Pientka, Alessandro Romito, Mathias Duckheim, Yuval Oreg, and Felix von Oppen. Signatures of topological phase transitions in mesoscopic superconducting rings. *New J. Phys.*, 15(2):025001, February 2013.

[33] Michael Hell, Martin Leijnse, and Karsten Flensberg. Two-Dimensional Platform for Networks of Majorana Bound States. *Phys. Rev. Lett.*, 118(10):107701, March 2017.

[34] Antonio Fornieri, Alexander M. Whiticar, F. Setiawan, Elías Portolés, Asbjørn C. C. Drachmann, Anna Keselman, Sergei Gronin, Candice Thomas, Tian Wang, Ray Kallaher, Geof-

frey C. Gardner, Erez Berg, Michael J. Manfra, Ady Stern, Charles M. Marcus, and Fabrizio Nichele. Evidence of topological superconductivity in planar Josephson junctions. *Nature*, 569(7754):89–92, May 2019.

[35] Hechen Ren, Falko Pientka, Sean Hart, Andrew T. Pierce, Michael Kosowsky, Lukas Lunczer, Raimund Schlereth, Benedikt Scharf, Ewelina M. Hankiewicz, Laurens W. Molenkamp, Bertrand I. Halperin, and Amir Yacoby. Topological superconductivity in a phase-controlled Josephson junction. *Nature*, 569(7754):93–98, May 2019.

[36] Benedikt Scharf, Falko Pientka, Hechen Ren, Amir Yacoby, and Ewelina M. Hankiewicz. Tuning topological superconductivity in phase-controlled Josephson junctions with Rashba and Dresselhaus spin-orbit coupling. *Phys. Rev. B*, 99(21):214503, June 2019.

[37] Tong Zhou, Matthieu C. Dartiailh, William Mayer, Jong E. Han, Alex Matos-Abiague, Javad Shabani, and Igor Žutić. Phase Control of Majorana Bound States in a Topological X Junction. *Phys. Rev. Lett.*, 124(13):137001, April 2020.

[38] Jin-Peng Xu, Mei-Xiao Wang, Zhi Long Liu, Jian-Feng Ge, Xiaojun Yang, Canhua Liu, Zhu An Xu, Dandan Guan, Chun Lei Gao, Dong Qian, Ying Liu, Qiang-Hua Wang, Fu-Chun Zhang, Qi-Kun Xue, and Jin-Feng Jia. Experimental Detection of a Majorana Mode in the core of a Magnetic Vortex inside a Topological Insulator-Superconductor Bi 2 Te 3 / NbSe 2 Heterostructure. *Phys. Rev. Lett.*, 114(1):017001, January 2015.

[39] S. M. Albrecht, A. P. Higginbotham, M. Madsen, F. Kuemmeth, T. S. Jespersen, J. Nygård, P. Krogstrup, and C. M. Marcus. Exponential protection of zero modes in Majorana islands. *Nature*, 531(7593):206–209, March 2016.

[40] Hao-Hua Sun, Kai-Wen Zhang, Lun-Hui Hu, Chuang Li, Guan-Yong Wang, Hai-Yang Ma, Zhu-An Xu, Chun-Lei Gao, Dan-Dan Guan, Yao-Yi Li, Canhua Liu, Dong Qian, Yi Zhou, Liang Fu, Shao-Chun Li, Fu-Chun Zhang, and Jin-Feng Jia. Majorana Zero Mode Detected

with Spin Selective Andreev Reflection in the Vortex of a Topological Superconductor. *Phys. Rev. Lett.*, 116(25):257003, June 2016.

[41] Dongfei Wang, Lingyuan Kong, Peng Fan, Hui Chen, Shiyu Zhu, Wenyao Liu, Lu Cao, Yujie Sun, Shixuan Du, John Schneeloch, Ruidan Zhong, Genda Gu, Liang Fu, Hong Ding, and Hong-Jun Gao. Evidence for Majorana bound states in an iron-based superconductor. *Science*, 362(6412):333–335, October 2018.

[42] Berthold Jäck, Yonglong Xie, Jian Li, Sangjun Jeon, B. Andrei Bernevig, and Ali Yazdani. Observation of a Majorana zero mode in a topologically protected edge channel. *Science*, 364(6447):1255–1259, June 2019.

[43] Sujit Manna, Peng Wei, Yingming Xie, Kam Tuen Law, Patrick A. Lee, and Jagadeesh S. Moodera. Signature of a pair of Majorana zero modes in superconducting gold surface states. *Proceedings of the National Academy of Sciences*, 117(16):8775–8782, April 2020.

[44] Geoffrey L. Fatin, Alex Matos-Abiague, Benedikt Scharf, and Igor Žutić. Wireless Majorana Bound States: From Magnetic Tunability to Braiding. *Phys. Rev. Lett.*, 117(7):077002, August 2016.

[45] Jay D. Sau and S. Das Sarma. Realizing a robust practical Majorana chain in a quantum-dot-superconductor linear array. *Nat Commun*, 3(1):964, July 2012.

[46] Martin Leijnse and Karsten Flensberg. Parity qubits and poor man's Majorana bound states in double quantum dots. *Phys. Rev. B*, 86(13):134528, October 2012.

[47] Tom Dvir, Guanzhong Wang, Nick van Loo, Chun-Xiao Liu, Grzegorz P. Mazur, Alberto Bordin, Sebastiaan L. D. ten Haaf, Ji-Yin Wang, David van Driel, Francesco Zatelli, Xiang Li, Filip K. Malinowski, Sasa Gazibegovic, Ghada Badawy, Erik P. A. M. Bakkers, Michael Wimmer, and Leo P. Kouwenhoven. Realization of a minimal Kitaev chain in coupled quantum dots. *Nature*, 614(7948):445–450, February 2023.

[48] Torsten Karzig, Christina Knapp, Roman M. Lutchyn, Parsa Bonderson, Matthew B. Hastings, Chetan Nayak, Jason Alicea, Karsten Flensberg, Stephan Plugge, Yuval Oreg, Charles M. Marcus, and Michael H. Freedman. Scalable designs for quasiparticle-poisoning-protected topological quantum computation with Majorana zero modes. *Phys. Rev. B*, 95(23):235305, June 2017.

[49] Andrew C. Potter and Patrick A. Lee. Multichannel Generalization of Kitaev's Majorana End States and a Practical Route to Realize Them in Thin Films. *Phys. Rev. Lett.*, 105(22):227003, November 2010.

[50] Jian Li, Titus Neupert, B. Andrei Bernevig, and Ali Yazdani. Manipulating Majorana zero modes on atomic rings with an external magnetic field. *Nat Commun*, 7(1):10395, January 2016.

[51] O. Pietzsch, S. Okatov, A. Kubetzka, M. Bode, S. Heinze, A. Lichtenstein, and R. Wiesendanger. Spin-Resolved Electronic Structure of Nanoscale Cobalt Islands on Cu(111). *Phys. Rev. Lett.*, 96(23):237203, June 2006.

[52] Alessandro Romito, Jason Alicea, Gil Refael, and Felix von Oppen. Manipulating Majorana fermions using supercurrents. *Phys. Rev. B*, 85(2):020502, January 2012.

[53] Kazuaki Takasan, Shuntaro Sumita, and Youichi Yanase. Supercurrent-induced topological phase transitions. *Phys. Rev. B*, 106(1):014508, July 2022.

[54] *See Supplemental Material at [url].*

[55] Jian Li, Hua Chen, Ilya K. Drozdov, A. Yazdani, B. Andrei Bernevig, and A. H. MacDonald. Topological superconductivity induced by ferromagnetic metal chains. *Phys. Rev. B*, 90(23):235433, December 2014.

[56] Tudor E. Pahomi, Manfred Sigrist, and Alexey A. Soluyanov. Braiding Majorana corner modes in a second-order topological superconductor. *Phys. Rev. Res.*, 2(3):032068, September 2020.

[57] Ryan V. Mishmash, Bela Bauer, Felix von Oppen, and Jason Alicea. Dephasing and leakage dynamics of noisy Majorana-based qubits: Topological versus Andreev. *Phys. Rev. B*, 101(7):075404, February 2020.

[58] Gábor Széchenyi and András Pályi. Parity-to-charge conversion for readout of topological majorana qubits. *Phys. Rev. B*, 101:235441, Jun 2020.

[59] Guan-Hao Feng and Hong-Hao Zhang. Probing robust Majorana signatures by crossed Andreev reflection with a quantum dot. *Phys. Rev. B*, 105(3):035148, January 2022.

[60] K. v. Klitzing, G. Dorda, and M. Pepper. New method for high-accuracy determination of the fine-structure constant based on quantized hall resistance. *Phys. Rev. Lett.*, 45(6):494–497, August 1980.

[61] K. S. Novoselov, A. K. Geim, S. V. Morozov, D. Jiang, M. I. Katsnelson, I. V. Grigorieva, Dubonos S. V., and A. A. Firsov. Two-dimensional gas of massless Dirac fermions in graphene. *Nature Physics*, 438:197, 2005.

[62] Yuanbo Zhang, Yan-Wen Tan, Horst L. Stormer, and Philip Kim. Experimental observation of the quantum Hall effect and Berry's phase in graphene. *Nature Physics*, 438:201, 2005.

[63] A. H. Castro Neto, F. Guinea, N. M. R. Peres, K. S. Novoselov, and A. K. Geim. The electronic properties of graphene. *Rev. Mod. Phys.*, 81(1):109–162, January 2009.

[64] Netanel H. Lindner, Gil Refael, and Victor Galitski. Floquet topological insulator in semiconductor quantum wells. *Nature Physics*, 7:490, 2011.

[65] André Eckardt and Egidijus Anisimovas. High-frequency approximation for periodically driven quantum systems from a Floquet-space perspective. *New J. Phys.*, 17:093039, 2015.

[66] Mikael C. Rechtsman, Julia M. Zeuner, Yonatan Plotnik, Yaakov Lumer, Daniel Podolsky, Felix Dreisow, Stefan Nolte, Mordechai Segev, and Alexander Szameit. Photonic floquet topological insulators. *Nature Physics*, 496:196, 2013.

[67] Y. H. Wang, H. Steinberg, P. Jarillo-Herrero, and N. Gedik. Observation of floquet-bloch states on the surface of a topological insulator. *Science*, 342(6157):453–457, 2013.

[68] Hongbin Zhang, Jiandong Yao, Jianmei Shao, Hai Li, Shuwei Li, Dinghua Bao, Chengxin Wang, and Guowei Yang. Anomalous photoelectric effect of a polycrystalline topological insulator film. *Scientific Reports*, 4:5876, 2014.

[69] J. W. McIver, B. Schulte, F.-U. Stein, T. Matsuyama, G. Jotzu, G. Meier, and A. Cavalleri. Light-induced anomalous Hall effect in graphene. *Nature Physics*, 11:123, 2019.

[70] Jon H. Shirley. Solution of the schrödinger equation with a hamiltonian periodic in time. *Phys. Rev.*, 138(4B):B979–B987, May 1965.

[71] Hideo Sambe. Steady states and quasienergies of a quantum-mechanical system in an oscillating field. *Phys. Rev. A*, 7(6):2203–2213, June 1973.

[72] Milena Grifoni and Peter Hänggi. Driven quantum tunneling. *Physics Reports*, 304:229, 1998.

[73] M. Bukov, L. Ď Alessio, and A. Polkovnikov. Universal high-frequency behavior of periodically driven systems: From dynamical stabilization to Floquet engineering. *Advances in Physics*, 64:139, 2015.

[74] N. Goldman and J. Dalibard. Periodically driven quantum systems: Effective hamiltonians and engineered gauge fields. *Phys. Rev. X*, 4(3):031027, August 2014.

[75] Saar Rahav, Ido Gilary, and Shmuel Fishman. Effective Hamiltonians for periodically driven systems. *Phys. Rev. A*, 68(1):013820, July 2003.

[76] A. P. Itin and M. I. Katsnelson. Effective hamiltonians for rapidly driven many-body lattice systems: Induced exchange interactions and density-dependent hoppings. *Phys. Rev. Lett.*, 115(7):075301, August 2015.

[77] Takahiro Mikami, Sota Kitamura, Kenji Yasuda, Naoto Tsuji, Takashi Oka, and Hideo Aoki. Brillouin-Wigner theory for high-frequency expansion in periodically driven systems: Application to Floquet topological insulators. *Phys. Rev. B*, 93(14):144307, April 2016.

[78] E. S. Mananga and T. Charpentier. Introduction of the Floquet-Magnus expansion in solid-state nuclear magnetic resonance spectroscopy. *The Journal of Chemical Physics*, 135:044109, 2011.

[79] T. Kuwahara, T. Mori, and K. Saito. Floquet–Magnus theory and generic transient dynamics in periodically driven many-body quantum systems. *Annals of Physics*, 367:96, 2016.

[80] A. López, A. Scholz, Z. Z. Sun, and J. Schliemann. Graphene with time-dependent spin-orbit coupling: Truncated Magnus expansion approach. *Eur. Phys. J. B*, 86:366, 2013.

[81] F. Casas, J. A. Oteo, and J. Ros. Floquet theory: Exponential perturbative treatment. *J. Phys. A*, 34:3379, 2001.

[82] Takuya Kitagawa, Takashi Oka, Arne Brataas, Liang Fu, and Eugene Demler. Transport properties of nonequilibrium systems under the application of light: Photoinduced quantum Hall insulators without Landau levels. *Phys. Rev. B*, 84(23):235108, December 2011.

[83] F. D. M. Haldane. Model for a quantum hall effect without landau levels: Condensed-matter realization of the "Parity Anomaly". *Phys. Rev. Lett.*, 61(18):2015–2018, October 1988.

[84] Andrei Kirilyuk, Alexey V. Kimel, and Theo Rasing. Ultrafast optical manipulation of magnetic order. *Rev. Mod. Phys.*, 82(3):2731–2784, September 2010.

[85] J. H. Mentink, K. Balzer, and M. Eckstein. Ultrafast and reversible control of the exchange interaction in Mott insulators. *Nature Communications*, 6:6708, 2015.

[86] L. Stojchevska, I. Vaskivskyi, T. Mertelj, P. Kusar, D. Svetin, S. Brazovskii, and D. Mihailovic. Ultrafast switching to a stable hidden quantum state in an electronic crystal. *Science*, 344(6180):177–180, 2014.

[87] Adolfo G. Grushin, Álvaro Gómez-León, and Titus Neupert. Floquet fractional chern insulators. *Phys. Rev. Lett.*, 112(15):156801, April 2014.

[88] Mark S. Rudner and Netanel H. Lindner. Floquet topological insulators: From band structure engineering to novel non-equilibrium quantum phenomena. *arxiv*.

[89] Ervand Kandelaki and Mark S. Rudner. Many-body dynamics and gap opening in interacting periodically driven systems. *Phys. Rev. Lett.*, 121(3):036801, July 2018.

[90] G. Juzeliūūnas and P. Öhberg. Slow light in degenerate fermi gases. *Phys. Rev. Lett.*, 93(3):033602, July 2004.

[91] J. Ruseckas, G. Juzeliūūnas, P. Öhberg, and M. Fleischhauer. Non-abelian gauge potentials for ultracold atoms with degenerate dark states. *Phys. Rev. Lett.*, 95(1):010404, June 2005.

[92] Shi-Liang Zhu, Hao Fu, C.-J. Wu, S.-C. Zhang, and L.-M. Duan. Spin hall effects for cold atoms in a light-induced gauge potential. *Phys. Rev. Lett.*, 97(24):240401, December 2006.

[93] Jean Dalibard, Fabrice Gerbier, Gediminas Juzeliūūnas, and Patrik Öhberg. Colloquium: Artificial gauge potentials for neutral atoms. *Rev. Mod. Phys.*, 83(4):1523–1543, November 2011.

[94] N Goldman, G Juzeliūnas, P Öhberg, and I B Spielman. Light-induced gauge fields for ultracold atoms. *Reports on Progress in Physics*, 77(12):126401, November 2014.